2016

Approximated Control Affine Dynamics Mode For an Agricultural Field Robot Considering Wheel Terrain Interaction

Pablo Menendez-Aponte
University of Central Florida, olbap323@gmail.com

APPROXIMATED CONTROL AFFINE DYNAMICS MODEL FOR AN AGRICULTURAL FIELD ROBOT CONSIDERING WHEEL TERRAIN INTERACTION

by

PABLO MENENDEZ-APONTE
B.S. University Of Central Florida, 2015

A thesis submitted in partial fulfillment of the requirements
for the degree of Master of Science
in the Department of Mechanical and Aerospace Engineering
in the College of Engineering and Computer Science
at the University of Central Florida
Orlando, Florida

Fall Term
2016

Major Professor:
Yunjun Xu

ABSTRACT

As populations and the demand for higher crop yields grow, so to does the need for efficient agricultural wheeled mobile robots. To achieve precise navigation through a field it is desirable that the control system is designed based on an accurate dynamic model. In this paper a control affine model for a custom designed skid-steer differential drive wheeled mobile robot is found. The Terramechanic wheel terrain interaction is adopted and modified to consider wheels with a torus geometry. Varying slip ratios and slip angles are considered in the terrain reaction forces, which is curve-fitted using a nonlinear least squares approach such that the achieved model is control affine. The parameters in the proposed model is identified through an extended Kalman filter so that the state variables in the model are matched. Both simulation and experiments in a commercial farm validated the proposed model and the identification approach.

ACKNOWLEDGMENTS

I would like to thank Dr. Yunjun Xu for pushing me to achieve more in my research as well has his constant help with any and all research tasks.

I would also like to thank the rest of the faculty and staff at University of Central Florida for helping me to expand my knowledge as well as helping me learn valuable engineering skills which I will carry with me forever.

I would also like to thank my parents, Sergio and Andrea Menedez-Aponte, and Alexandra Riley for their support and patience while I pursued my dream of higher education.

I would like to thank my labmates who helped me on this project, Carlos Merchan, Christian Garcia, Kenneth Thompson, Douglas Freese and Sinem Defterli.

I would also like to thank Dr. Faissal Moslehy and Dr. Kurt Lin for being on my thesis committee.

TABLE OF CONTENTS

LIST OF FIGURES

LIST OF TABLES

CHAPTER 1

INTRODUCTION

Emerging robotic automation techniques in agriculture has become the focus of much attention. Robotics in agriculture could be used as a means to reduce labor costs, enhance farming efficiency and increase profitability. A private research company, WinterGreen research, published a study entitled Agricultural Robots Market Shares, Worldwide, 2014 to 2020 where they predict that the agricultural robot market will expand from $817 million in 2013 to $16.3 billion by 2020. Furthermore, WinterGreen research predicts that while many unmanned aerial vehicles have been put to use in research, autonomous wheeled mobile robots will in the end be the more useful mode of robotics in this field [1].The growth in agricultural mobile robotics are predicted because of the large scale of commercial agricultural fields, which limits the amount of crop a human laborer can feasibly get to by foot in a normal eight-hour work day and increases the likelihood of error due to fatigue. Furthermore, the structured nature of the commercial agricultural fields makes them ideal for robotic scouts that can efficiently work long hours over large distances. Autonomous robotics could enhance farm productivity in every stage of a crops cultivation from harvesting to planting and everything in between. In recent years many advances in robotics are closing the technological gap required to make agricultural mobile robots a feasible goal.

For instance, low cost ultrasonic range finders were utilized in the design of a row guidance system for an autonomous robot for white asparagus harvesting at the Institute of Mobile Systems in Germany[2]. Machine vision has opened the door for new capabilities of estimation algorithms as shown by the development of a strawberry harvester at the Institute of Agricultural Machinery in Japan[3],and a corn nitrogen deficiency detector at University of Tehran in Iran[4]. Another sub field of machine vision, spectroscopic imaging, has emerged as a means of rapid disease detection in agriculture and is drawing attention as a new potential for wheeled mobile robots in agriculture[5]. As of 2001 a study has shown that plant pathogen account for a 33 billion-dollar loss in agricultural revenue in the US alone[6].Despite these advances there are still problems that must be solved before fully automated agriculture can be realized. One critical advancement in off-road robotics that remains to be a fully matured area of research is dynamic modeling of mobile robots in loose terrain. While there are many techniques for the design of wheeled vehicles in loose terrain theyre are computationally expensive and not suitable for control.

In the past, control and localization schemes for wheeled mobile robots traveling on hard surfaces have been accomplished using no-slip non-holonomic wheel constraints and wheel odometry[7].Researchers have been able to successfully apply the traditional no slip constraints to autonomous tasks in agriculture as in [2], where the robot was not required to do any radical maneuvers and a high fidelity position measurement was available. If sharp turns are to be made, a navigation estimation scheme is being designed or the slipping and skidding are inherent to the robot design (as in a skid-steer robot) traditional models

fail. In general, in loose terrain terrain wheel slip ratio and slip angle play a critical role in the dynamics of wheeled mobile robots of all configurations and must be accounted for. In[8] and [9].the authors use a kinematic constraint for a four-wheel skid steer robot that is borrowed from design of treaded ground vehicles. This constraint uses data collected experimentally to relate the slip/skid ratio to the yaw rate of the vehicle. While these authors have shown success using experimental kinematics, the constraints are purely empirical and have no physical foundation making them unpredictable for new terrains. Furthermore, they completely neglect slip angle.

The research conducted in this paper was carried out with the goal of a robotic strawberry orchard scout in mind. The realization of a robotic scout for disease detection in strawberry orchards has several control system design criteria that have not been addressed by previous research works. Commercial strawberry orchards are grown in organized plasticulture rows that can range in size and spacing. From the authors experience in three commercial fields in Florida the beds generally range in size from 23-28 inches and are spaced 18-22 inches apart. These dimensions will require a turn with a turning radius of approximately 32 inches or 80 centimeters during cross-the-bed maneuvers. Additionally, the three leading states for strawberry production, California, Florida and Oregon [10], have different climates and topology. With this in mind this paper presents an approximate wheel terrain interaction model (WTIM) suitable for control under tight turns when slipping/skidding are at their highest and furthermore present a parameter estimation scheme to adapt to new environments.In this paper a wheeled mobile robot modeling approach based

purely in the physics and not kinematics was sought after. We begin with the Terramechanic WTIM, first developed in the fifties by M.G. Bekker and later on by J.Y. Wong [11],[12].The Terramechanic WTIM has become a popular means for off road vehicle design due to its accuracy and reduction in computational cost when compared with finite element methods. In terms of control however, Terramechanic WTIMs are not analytical and thus cannot be implemented in control and guidance estimation algorithms. Here Terramechanic WTIMs are utilized to gain a more fundamental understanding of the dominant forces that characterize mobile robot dynamics in off road terrains. This knowledge is applied to find an approximate WTIM that can be used for control and navigation. The analytic model is then fit into an appropriate Kalman filter estimation scheme for online parameter estimation.

This paper is organized as followed. In section II the rigid body dynamics for an agricultural field robot are derived. We begin in part A with a general formulation of the rigid body dynamics of a rover traveling on a plane. In part B a Terramechanic method for estimating the terrain reaction force on a torus shaped wheel is presented and integrated in the dynamics from part A. Section III part A explores an analytical approximate wheel terrain interaction model which renders the final rover model, presented in B, control affine. In section IV the analytic wheel terrain interaction model from part III is fit into an extended Kalman filter for on line parameter estimation. The parameter estimation scheme and thus the analytic model is validated through experiments on a real commercial strawberry farm in section V.

CHAPTER 2

SKID-STEER KINEMATICS AND GENERAL 2-D DYNAMICS

2.1 Reference Frames

Kinematic and dynamics models are developed for a custom skid-steer field robot designed for strawberry orchards. A diagram of the field robot is shown in Fig. 2.1. The robot is assumed to travel on a fixed horizontal plane, thus the complete posture of the robot can be defined in an inertial reference frame by two position coordinates (x_i, y_i) and the heading angle (ψ_R),where the subscript i denotes the inertial reference frame located at an arbitrary stationary position in space and the subscript R denotes an additional body fixed robot reference frame placed at the center of mass of the robot. Accompanying the inertial and body fixed frame are four local wheel reference frames,$(x_i, y_i), i = 1, 2, 3, 4$. The local wheel reference frames are fixed in, and have the same orientation as the body reference frame. The distance from the origin of the body fixed reference frame to the i_{th} wheel local reference frame origin is denoted by the position vector $\vec{\rho}_i$.The distance W is the distance from the robot center of mass to the wheel center of mass along the body fixed y-axis, likewise L refers to the distance from the robot center of mass to the wheel center of mass along the body fixed x-axis.

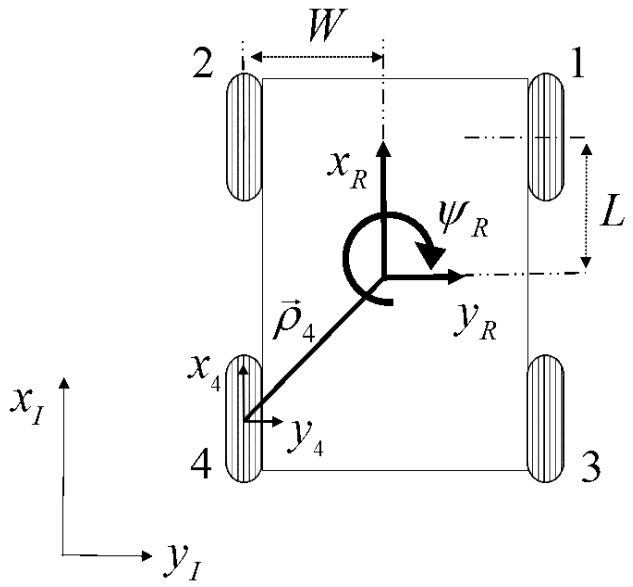

Figure 2.1: View of robot displaying the inertial and body fixed coordinates.

2.2 Skid-Steer Kinematics

Some useful notation that will be used later on in the paper are included here. The wheels are divided into right and left wheel banks for example, the right wheel bank of the four wheeled skid-steer robot shown in Fig. 2.1 will consist of wheels 1 and 3, whereas the left wheel bank will consist of wheels 2 and 4. As opposed to separate descriptions for each wheel some of the wheel kinematics can be described in terms of the wheel banks. For instance, all wheels on a certain wheel bank have the same angular velocity (ω). The right and left wheel bank angular velocities

$$\omega_r = \omega_1 = \omega_3 \tag{2.1}$$

$$\omega_l = \omega_2 = \omega_4 \tag{2.2}$$

The longitudinal velocities of the right and left wheel bank can be written in their respective local reference frames similar to the angular velocities

$$\dot{x}_r = \dot{x}_1 = \dot{x}_3 = \dot{x}_R + W\dot{\psi}_R \tag{2.3}$$

$$\dot{x}_l = \dot{x}_2 = \dot{x}_4 = \dot{x}_R - W\dot{\psi}_R \tag{2.4}$$

2.3 Equation Of Motion

Now we define the general equations of motion for a rigid body on a plane. We begin with the kinematics, the direction cosine matrix from the inertial frame to the body frame is

$$\boldsymbol{R_1} = \begin{bmatrix} \cos(\psi_R) & -\sin(\psi_R) \\ \sin(\psi_R) & \cos(\psi_R) \end{bmatrix} \tag{2.5}$$

Let $(\dot{x}_R, \dot{y}_R, \dot{\psi}_R)$ be the longitudinal, lateral and angular velocity of the robot in the body fixed frame, and $(\dot{x}_I, \dot{y}_I, \dot{\psi}_R)$ be the robot velocities in the inertial frame. Note that for motion on a plane the yawing velocity is the same in both frames [dynamics ref.]. Then the inertial velocity can be expressed by the robot velocities in the body frame as

$$\begin{bmatrix} \dot{x}_I \\ \\ \dot{y}_I \end{bmatrix} = \boldsymbol{R_1} \begin{bmatrix} \dot{x}_R \\ \\ \dot{y}_R \end{bmatrix} \tag{2.6}$$

, and the acceleration can be expressed as

$$\frac{d}{dt}\begin{bmatrix}\dot{x}_I \\ \\ \dot{y}_I\end{bmatrix} = \frac{d}{dt}\left\{\boldsymbol{R_1}\begin{bmatrix}\dot{x}_R \\ \\ \dot{y}_R\end{bmatrix}\right\} \tag{2.7}$$

which leads to

$$\begin{bmatrix}\ddot{x}_I \\ \\ \ddot{y}_I\end{bmatrix} = \boldsymbol{R_1}\begin{bmatrix}\ddot{x}_R - \dot{\psi}_R\dot{y}_R \\ \\ \ddot{y}_R + \dot{\psi}_R\dot{x}_R\end{bmatrix} \tag{2.8}$$

Now we can form the equations of motions using Newtons Second law of motion.

$$\begin{aligned}\tfrac{d}{dt}\{ma_x\} &= \textstyle\sum F_{ext,x} \\ \tfrac{d}{dt}\{ma_y\} &= \textstyle\sum F_{ext,y} \\ \tfrac{d}{dt}\{I\alpha\} &= \textstyle\sum M_{ext}\end{aligned} \tag{2.9}$$

Where a_x,a_y and α are the absolute acceleration of the robot in the body fixed frame i.e. $a_x = \ddot{x}_R - \dot{\psi}_R\dot{y}_R$,$a_y = \ddot{y}_R + \dot{\psi}_R\dot{x}_R$ and $\alpha = \ddot{\psi}_R$. Also the external forces acting on the robot are $F_{ext,x}$ and $F_{ext,y}$ in the body fixed frame, whereas the external moments acting on the body are denoted by M_{ext}, again in the body fixed frame. The mass of the robot is denoted by m and the moment of inertia along the principle z-axis is I, both of which are time invariant. Thus general equations of motion formulated in the body frame are expressed as.

$$\begin{aligned}\ddot{x}_R &= \dot{\psi}_R\dot{y}_R + \textstyle\sum F_{ext,x}/m \\ \ddot{y}_R &= -\dot{\psi}_R\dot{x}_R + \textstyle\sum F_{ext,x}/m \\ \ddot{\psi}_R &= \textstyle\sum M_{ext}/I\end{aligned} \tag{2.10}$$

For agricultural scouting, high speed maneuvering is not required thus constant wheel loads are assumed and aerodynamic forces are neglected. The applied forces and moment $\sum F_{ext,x}$, $\sum F_{ext,y}$ and $\sum M_{ext}$ are the summation of the forces and moment produced at each wheel of the vehicle by the wheel terrain interaction.

CHAPTER 3

INDIVIDUAL WHEEL TERRAIN INTERACTION MODELS (WTIM)

3.1 Terramechanics Model for Wheel Terrain Interaction

Now the terrain reaction on an individual wheel, referred to as the Wheel Terrain Interaction Model (WTIM), is developed, mainly using the terramechanic method [13]. In the past, terramechanic models have been utilized in the design of terrestrial rovers which use wheels with a cylindrical type of geometry [14]. For a typical agricultural field robot, the wheel has a torus or donut geometry. In computation, the torus geometry has an advantage over the cylindrical geometry in that bulldozing forces must be considered when using the cylindrical terramechanic model [13],[14].The disadvantage of the torus geometry however is that the surface requires two rotations which adds to the complexity of the integral that must be computed for the terrain reaction. This section focuses on the WTIM for an individual wheel thus, for clarity and brevity the subscript associated with wheels 1, 2, 3, and 4 are omitted in this section.

3.1.1 Torus Geometry and Sinkage Depth

A torus is a surface of revolution generated by revolving an ellipse around an axis coplanar with the ellipse. Defining a wheel reference frame with its origin in the center of the torus (i.e. the wheel hub), the torus surface can be expressed parametrically by the position vector $\vec{r}$ from the center of mass of the wheel [15], as shown in Fig.3.1.

$$\boldsymbol{r}(\theta,\psi) = \begin{Bmatrix} (c + a\cos(\psi))\sin(\theta) \\ b\sin(\psi) \\ (c + a\cos(\psi))\cos(\theta) \end{Bmatrix} \tag{3.1}$$

where c is the major radius, a is the minor radius, b is half of the torus width, and the angles of revolution are θ and ψ as shown in Fig. 3.1. For convenience two unit vectors are defined. The first unit vector, $\begin{Bmatrix} \hat{i} & \hat{j} & \hat{k} \end{Bmatrix}^T$, is fixed and is oriented with the wheel reference frame. The second system, $\begin{Bmatrix} \hat{t} & \hat{l} & \hat{n} \end{Bmatrix}^T$, describes the tangent, lateral and normal directions of the wheel surface at any arbitrary surface point. The surface unit vector can be found using.

$$\boldsymbol{r} = \boldsymbol{r}/|\boldsymbol{r}| \; = \begin{Bmatrix} \hat{t} & \hat{l} & \hat{n} \end{Bmatrix}^T \tag{3.2}$$

At this point the sinkage depth,N_z,can be defined as the distance the wheel penetrates the terrain. The sinkage depth defines the contact patch or the region of the wheel surface that makes contact with the terrain. As will be seen in the derivation of the terramechanic WTIM model, it is convenient to describe the contact patch by four angles: the entry angle θ_f, exit angle θ_r, right bound angle ψ_r and left bound angle ψ_l.

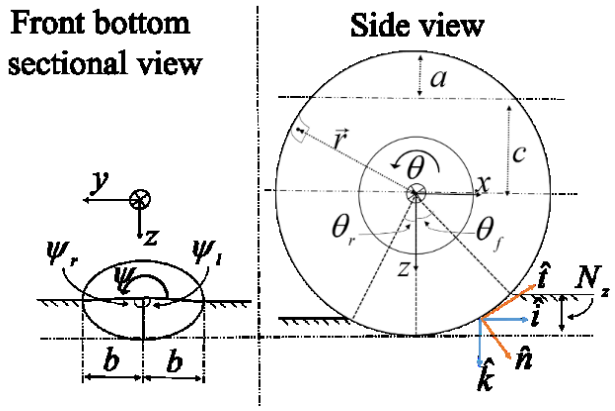

Figure 3.1: View of robot displaying the inertial and body fixed coordinates.

3.1.2 Derivation

The general theory behind Terramechanic wheel terrain interaction models is that the force acting on a steadily rotating wheel, $\begin{Bmatrix} F_{w,x} & F_{w,y} & F_{w,z} \end{Bmatrix}^T$, can be found by integrating the radial, tangential, and lateral stress components along the wheel-terrain contact patch [11], [12], [16].

$$\boldsymbol{F}_w = \iint_R \boldsymbol{p} dS \tag{3.3}$$

where R is the contact patch region and the pressure vector field is denoted by $\vec{p}$. The infinitesimal surface increment dS can be computed by [15]

$$dS = |\partial \boldsymbol{r}/\partial\psi \ \times \partial \boldsymbol{r}/\partial\theta \,| \, d\theta d\psi \tag{3.4}$$

In Eq. ((3.3)) the pressure vector,$\boldsymbol{p}$, is oriented with the wheel reference frame along the $\begin{Bmatrix} \hat{i} & \hat{j} & \hat{k} \end{Bmatrix}^T$ unit vector as

$$\boldsymbol{p} = \begin{bmatrix} p_x & p_y & p_z \end{bmatrix}^T \tag{3.5}$$

However, Terramechanic theory gives the stresses oriented along the wheel surface. In other words, the pressure vector at each point along the wheel surface is found along the $\begin{Bmatrix} \hat{t} & \hat{l} & \hat{n} \end{Bmatrix}^T$ unit vector (see Figure 3.1)

$$\boldsymbol{p_s} = \begin{bmatrix} \tau_t & \tau_l & \sigma_n \end{bmatrix}^T \tag{3.6}$$

where the terms τ_t, τ_l and σ_n are the tangent, lateral and radial stress components to the wheel surface. As follows a rotation, a sequence must be established between the unit vector for the central coordinate system placed at the wheel hub and the wheel surface coordinate-system.

$$\boldsymbol{R_2} = \begin{bmatrix} 1 & 0 & 0 \\ 0 & \cos(\psi) & \sin(\psi) \\ 0 & -\sin(\psi) & \cos(\psi) \end{bmatrix} \begin{bmatrix} \cos(\theta) & 0 & -\sin(\theta) \\ 0 & 1 & 0 \\ \sin(\theta) & 0 & \cos(\theta) \end{bmatrix} \tag{3.7}$$

Using Eqs. 3.3, (3.4) and (3.7) the integral that must be solved for to acquire the soil reaction force vector is written as

$$\boldsymbol{F}_w = \iint \left\{ R_2^T \vec{p}_s \right\} |\partial\vec{r}/\partial\psi \times \partial\vec{r}/\partial\theta \, | \, d\theta d\psi \tag{3.8}$$

$$F_{w,x} = \int_{\psi_l}^{\psi_r} \int_{\theta_r}^{\theta_f} \left[\left(\cos\left(\theta\right) \tau_t + \sin\left(\psi\right) \cos\left(\theta\right) \tau_l + \cos\left(\psi\right) \sin\left(\theta\right) \sigma_n \right) d \right] d\theta d\psi \tag{3.9}$$

$$F_{w,y} = \int_{\psi_l}^{\psi_r} \int_{\theta_r}^{\theta_f} \left[\left(\cos\left(\psi\right) \tau_l - \sin\left(\psi\right) \sigma_n \right) d \right] d\theta d\psi \tag{3.10}$$

and

$$F_{w,z} = \int_{\psi_l}^{\psi_r} \int_{\theta_r}^{\theta_f} \left[\left(-\sin\left(\theta\right) \tau_t + \sin\left(\psi\right) \cos\left(\theta\right) \tau_l + \cos\left(\psi\right) \cos\left(\theta\right) \sigma_n \right) d \right] d\theta d\psi \tag{3.11}$$

in which $d \triangleq \left(c + a\cos\left(\psi\right)\right) \sqrt{a^2 \sin^2\left(\psi\right) + b^2 \cos^2\left(\psi\right)}$

The computation of τ_t,τ_l and σ_n are based on [13],[16]. For clarity, a brief derivation of the stress components is listed in the appendix.

3.1.3 Terramechanics WTIM Simulation

As is customary in WTIM, the effects of while slip/skid λ and slip angle β on the longitudinal and lateral terrain reaction forces were investigated for a wheel under constant loading. The wheel slip/skid ratio is written as the ratio of the relative speed over the expected speed.

$$\lambda = \begin{cases} \left[-\left(c + a\right)\omega - \dot{x} \right] / \left(c + a\right)\omega & , |\dot{x}| \leq |\left(c + a\right)\omega| \\ \left[-\left(c + a\right)\omega - \dot{x} \right] / \dot{x} & , |\dot{x}| > |\left(c + a\right)\omega| \end{cases} \tag{3.12}$$

where the numerator is the difference between the ideal wheel velocity under no slipping or skidding and the actual wheel velocity. In the first term of the numerator the parameters c and a are the major and minor radii respectively, whereas ω is the individual wheel angular velocity and $\dot{x}$ is the wheel longitudinal velocity written in the wheel hub reference frame (Fig. 3.1). The author would like to clear up two potential confusions in the ideal wheel velocity term of the numerator. First the orientation of the wheel reference dictates that positive angular velocity of the wheel corresponds to negative linear velocity along the x-axis (as shown in Fig. 3.1) and second, the distance $c+a$ is simply the maximum radii of the wheel. Thus on a hard surface under no slip conditions the expected longitudinal velocity of a wheel is

$$\dot{x} = -\left(c + a\right)\omega \tag{3.13}$$

The wheel slip angle denoted by β is the angle made between the longitudinal and lateral velocity components of the wheel. Slip angle can be found using the geometric relationship

$$\beta = \arctan\left(\dot{y}/\dot{x}\right) \tag{3.14}$$

The velocities $\dot{(y)}$ and $\dot{(x)}$ are the velocity of the individual wheel.

The soil parameters used to simulate the off-road environments were taken from [17] and are and are tabulated in the appendix. The trends in the reaction force found in Fig.

3.2a and Fig. 3.2b are used in the next section to formulate an approximate WTIM that is suitable to derive a control affine model.

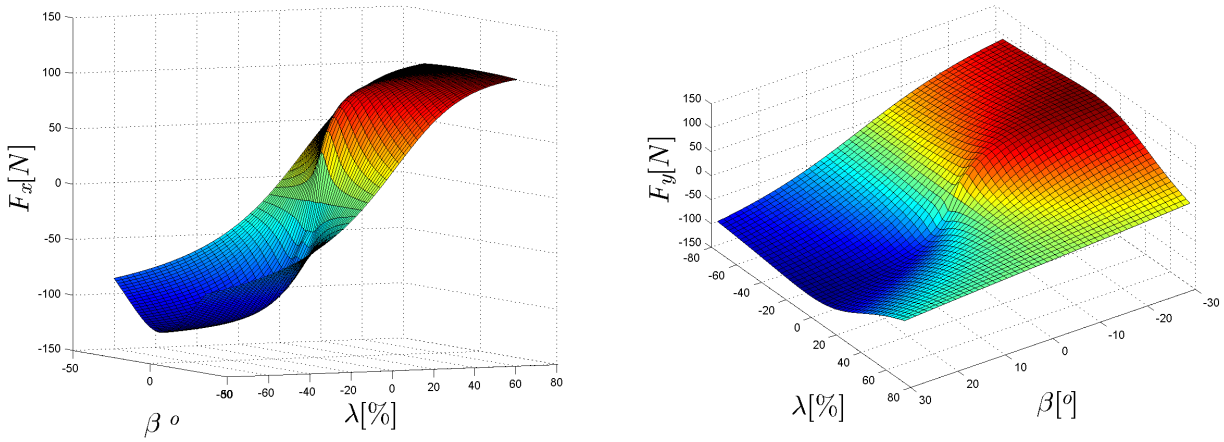

(a) Longitudinal reaction force

(b) Lateral reaction force

Figure 3.2: Terrain reaction predicted by Terramechanic WTIM

3.2 Approximate WTIM Simulation

While the terramechanic model allows for accurate simulations and quick analyses of the dominant forces of a wheeled vehicle in soft terrains, it does not have a control affine format and thus is not convenient for purposes of guidance, navigation, and control designs.

A large body of research has shown that the slip/skid ratio(λ) and the slip angle (β)are the critical elements of motion in off-road wheel terrain interactions [8],[9], [13],[14],[16], [17], [18], [19], [20]. In this study, the tangent force acting on a wheel is formulated as a function of slip and the lateral reaction force is formulated as a function of slip angle.

From 3.2a and the results found in [13], [14], [16] it is evident that although the tangent terrain reaction force lessens in magnitude with increasing magnitude of slip angle, it is primarily a function of slip and can be modeled with an exponentially decaying rate.

$$F_{w,x} \approx sign\,(\lambda)\left[1 - e^{-a_2|\lambda|}\right] \tag{3.15}$$

Equation(3.15) has advantages over the models presented in [9], [12] in that it does not require a separate formulation in the critical slip region. Additionally the model in [19] considers the tangential traction and rolling resistance as two different forces creating a large cumbersome formulation. The relationship in Eq.(3.15) is unified over the entire slip/skid ratio operating conditions and is easily defined by only two parameters.

Similarly, as shown by the terramechanic model in Fig. 3.2b, the lateral reaction force of the terrain on the wheel is primarily a function of the slip angle. Although it decays in the direction of increasing slip we have found good results using the formulation

$$F_{w,y} \approx -b\beta \tag{3.16}$$

Using a generated terramechanic data set with more than 2,500 points over the slip ratio range $\lambda \in [-1, 1]$ and the slip angle range$\beta \in \left[-\frac{\pi}{3}, \frac{\pi}{3}\right]$ in combination with MATLAB's *lsqcurvefit*algorithm, the parameters are approximated and the results are shown below. **Remark 1:**Based on the simulation results shown in Fig 3.3a and 3.3b , in the working range of $\lambda \in [-30\%, 30\%]$ and $\beta \in [-\pi/7, \pi/7]$, the error between the approximated force model and the actual WTIM model is between $[0\%, 42\%]$ in the longitudinal direction and between $[0\%, 45\%]$ in the lateral direction within the operating range of the robot wheels

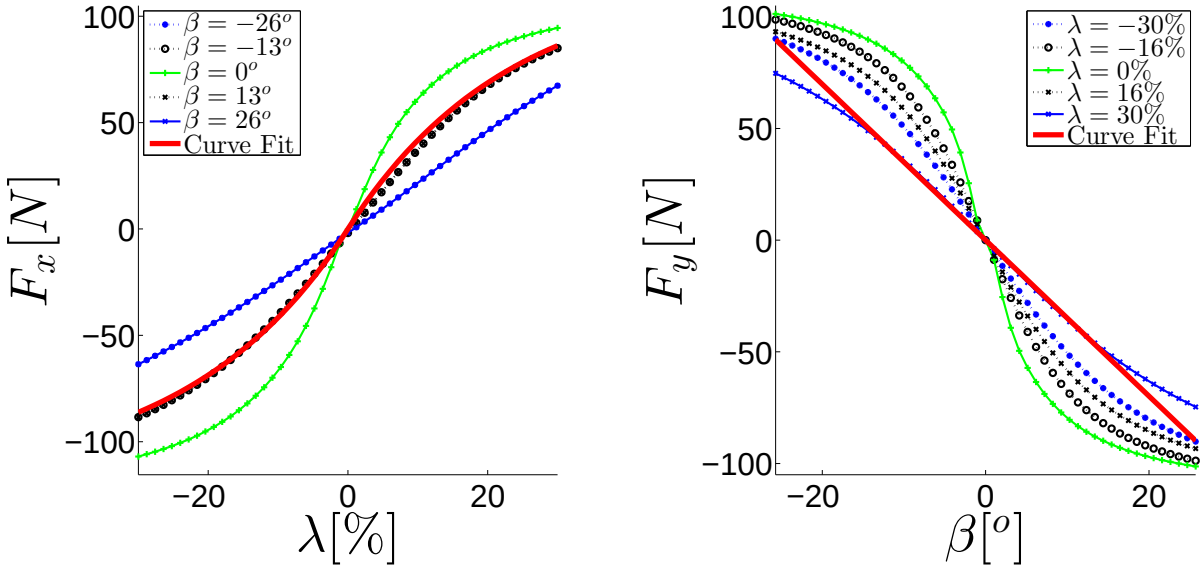

(a) Longitudinal reaction force

(b) Lateral reaction force

Figure 3.3: Terrain reaction predicted by approximate WTIM

CHAPTER 4

APPROXIMATED CONTROL AFFINE MODEL

The equations of motion for a four-wheel skid-steer style ground robot can now be given in the form of a nonlinear, state space, control affine model as

$$\dot{\boldsymbol{x}} = \boldsymbol{f}(\boldsymbol{x}) + \boldsymbol{g}(\boldsymbol{x})\boldsymbol{u} \tag{4.1}$$

the state vector is chosen as

$$x = \begin{bmatrix} \dot{x}_R & \dot{y}_R & \dot{\psi}_R & \omega_r & \omega_l & \lambda_r & \lambda_l & \beta_1 & \beta_2 & \beta_3 & \beta_4 \end{bmatrix}^T \tag{4.2}$$

As stated previously, the right and left wheel banks have equal angular and longitudinal velocities. Likewise, since the slip ratio is dependent only on the wheel longitudinal and angular velocities, then the slip for all four wheels of a skid-steer robot can be written succinctly as two slip ratios. Using Eqs. (2.1), (2.2), (2.3), (2.4) and (3.12) the left and right slip/skid ratio is expressed as

$$\lambda_j = \begin{cases} [(c+a)\,\omega_j - \dot{x}_j]/(c+a)\,\omega_j \;, |\dot{x}_j| \leq |(c+a)\,\omega_j| \\ [(c+a)\,\omega_j - \dot{x}_j]/\dot{x}_j \;, |\dot{x}_j| > |(c+a)\,\omega_j| \end{cases}, j = r, l \tag{4.3}$$

Now each element of the state vector ((4.2))can be described: the first three states with subscript R are the longitudinal, lateral, and yaw velocities of the robot in the body fixed

frame. The fourth and fifth element are the right and left wheel bank angular velocities. The following two states are the right and left longitudinal slip ratios and the remaining four states are the slip angles of each wheel.

The derivation of the state equations from the previously discussed equations, including the approximate wheel terrain interaction model, can now be presented. The state equations for the robot velocities are found from the equations of motion for a ground robot on a plane ((2.10)). Where the forces are the summation of the approximate terrain reaction forces (Eqs.(3.15)and (3.16))on each of the four wheels.

$$\sum F_{ext,x} = \sum_{i=1}^{4} F_{w,x,i} \tag{4.4}$$

$$\sum F_{ext,y} = \sum_{i=1}^{4} F_{w,y,i} \tag{4.5}$$

The subscript i denotes the wheel at which the force is being evaluated. Plugging Eq. (4.4) and (4.5) in (2.10) results in.

$$\ddot{x}_R = \dot{\psi}_R \dot{y}_R + \frac{2a_1}{m}\left[sign\left(\lambda_l\right) + sign\left(\lambda_r\right) - e^{-a_2|\lambda_r|} - e^{-a_2|\lambda_l|}\right] \tag{4.6}$$

$$\ddot{y}_R = -\dot{\psi}_R \dot{x}_R + \frac{b}{m}\sum_{i=1}^{4} \beta_i \tag{4.7}$$

Treating the terrain reaction as a point force acting at the center of the wheel the yawing moment is given by the summation of moments produced at each wheel

$$\boldsymbol{M} = \sum_{i=1}^{4} \boldsymbol{\rho_i} \times \boldsymbol{F_{w,i}} \tag{4.8}$$

where the position vector $\boldsymbol{\rho_i}$ is the position of the wheels center of mass relative to the rovers center of mass (Fig. 2.1). The force vector, $\boldsymbol{F_{w,i}}$, is the force produced at the wheel

expressed in terms of the rovers center of mass axis system. Plugging the relative distance vector ($\boldsymbol{\rho}_i, i = 1, 2, 3, 4$ - Fig. (2.1))and the approximate wheel terrain interaction forces (Eqs. (3.15) - (3.16)) into Eq. (4.8) leads to

$$\sum M_{ext} = 2W\left(F_{x,w,l} - F_{x,w,r}\right) + L\left(F_{y,w,1} + F_{y,w,2} - F_{y,w,3} - F_{y,w,4}\right) \tag{4.9}$$

Thus the yawing state equation is

$$\ddot{\psi}_R = \frac{2Wa_1}{I}\left[sign\left(\lambda_l\right) - sign\left(\lambda_r\right) - e^{-a_2|\lambda_l|} + e^{-a_2|\lambda_r|}\right] + \frac{Lb}{I}\left[\beta_1 + \beta_2 - \beta_3 - \beta_4\right] \tag{4.10}$$

Note that in Eqs. (4.9) and (4.10) we have utilized the fact that the longitudinal forces are a function of only the wheel slip/skid ratio and therefore the wheels on each bank will have the same longitudinal force, namely that $F_{w,x,1} = F_{w,x,3} = F_{w,x,r}$ and that $F_{w,x,2} = F_{w,x,4} = F_{w,x,l}$.

The angular velocities of each wheel bank are regulated by well-tuned PID controllers. System identification exercises suggest that the wheel bank angular velocities are related to the commanded velocity, $\omega_{c,j}$, by a first order differential equation as

$$\dot{\omega}_j = k_\omega\left(\omega_{c,j} - \omega_j\right), \qquad j = r, l \tag{4.11}$$

where k_ω is a motor time constant that was found experimentally to match the real system performance.

The state equations for the right and left wheel slip/skid ratio are found by taking the time derivatives of Eq.(4.3) which can be split into two parts: one which is related to and the other which is not related to the control input u.

$$\dot{\lambda}_j = f_{\lambda,j} + g_{\lambda,j}\omega_{c,j}, \qquad j = r, l \tag{4.12}$$

in which

$$f_{\lambda,j} = \begin{cases} \frac{-[\ddot{x}_j + v_{x,j} k_\omega]}{(c+a)\omega_j} & \dot{x}_j \leq (c+a)\,\omega_j \\ \frac{-(c+a)\omega_j [\dot{x}_j k_\omega - \ddot{x}_j]}{(\dot{x}_j)^2} & \dot{x}_j > (c+a)\,\omega_j \end{cases} \qquad j = r, l \tag{4.13}$$

and

$$g_{\lambda,j} = \begin{cases} \frac{\dot{x}_j (c+a) k_\omega}{((c+a)\omega_i)^2} & \dot{x}_j \leq (c+a)\,\omega_j \\ \frac{\dot{x}_j (c+a) k_\omega}{(\dot{x}_j)^2} & \dot{x}_j > (c+a)\,\omega_j \end{cases} \qquad j = r, l \tag{4.14}$$

The state equation for the slip angle can be found by taking the time derivative of (3.14) as

$$\dot{\beta}_i = \left(\dot{x}_i \ddot{y}_i - \dot{y}_i \ddot{x}_i\right) / \left(\dot{y}_i^2 + \dot{x}_i^2\right) \tag{4.15}$$

In Eq. (4.15), the symbols $\dot{x}_i$ are replaced by (2.3) for wheels 1 and 3 and Eq. (2.4) for wheeels 2 and 4. The symbols $\dot{y}_i,\ \ddot{x}_i,\ \ddot{y}_i$ are the lateral velocity and the longitudinal and lateral accelerations of the i^{th} wheel relative to the inertial frame. They can be found using the kinematic relationships.

$$\dot{y}_1 = \dot{y}_2 = \dot{y}_R + L\dot{\psi}_R \tag{4.16}$$

$$\dot{y}_3 = \dot{y}_4 = \dot{y}_R - L\dot{\psi}_R \tag{4.17}$$

$$\ddot{x}_r = \ddot{x}_1 = \ddot{x}_3 = \ddot{x}_R + W\ddot{\psi}_R \tag{4.18}$$

$$\ddot{x}_l = \ddot{x}_2 = \ddot{x}_4 = \ddot{x}_R - W\ddot{\psi}_R \tag{4.19}$$

$$\ddot{y}_1 = \ddot{y}_2 = \ddot{y}_R + L\ddot{\psi}_R \tag{4.20}$$

and

$$\ddot{y}_3 = \ddot{y}_4 = \ddot{y}_R - L\ddot{\psi}_R \tag{4.21}$$

The control input, u, is then selected as the nominal commanded wheel velocity

$$\boldsymbol{u} = \begin{bmatrix} \omega_{c,r} & \omega_{c,l} \end{bmatrix}^T \tag{4.22}$$

Equations (4.6), (4.7), (4.10), (4.11), (4.12) and (4.15) can be rearranged to produce the detailed state function in Eq. (4.1) as

$$\boldsymbol{f}(\boldsymbol{x}) = \begin{bmatrix} \dot{\psi}_R \dot{y}_R + \frac{2a_1}{m}\left[sign(\lambda_l) + sign(\lambda_r) - e^{-a_2|\lambda_r|} - e^{-a_2|\lambda_l|}\right] \\ -\dot{\psi}_R \dot{x}_R + \frac{b}{m}\sum_{i=1}^{4}\beta_i \\ \frac{2Wa_1}{I}\left[sign(\lambda_l) - sign(\lambda_r) - e^{-a_2|\lambda_l|} + e^{-a_2|\lambda_r|}\right] + \frac{Lb}{I}\left[\beta_1 + \beta_2 - \beta_3 - \beta_4\right] \\ -k_\omega \omega_r \\ -k_\omega \omega_l \\ f_{\lambda,r} \\ f_{\lambda,l} \\ (\dot{x}_1\ddot{y}_1 - \dot{y}_1\ddot{x}_1)/(\dot{y}_1^2 + \dot{x}_1^2) \\ (\dot{x}_2\ddot{y}_2 - \dot{y}_2\ddot{x}_2)/(\dot{y}_2^2 + \dot{x}_2^2) \\ (\dot{x}_3\ddot{y}_3 - \dot{y}_3\ddot{x}_3)/(\dot{y}_3^2 + \dot{x}_3^2) \\ (\dot{x}_4\ddot{y}_4 - \dot{y}_4\ddot{x}_4)/(\dot{y}_4^2 + \dot{x}_4^2) \end{bmatrix} \tag{4.23}$$

and the following control input matrix

$$\boldsymbol{g}(\boldsymbol{x}) = \begin{bmatrix} 0 & 0 \\ 0 & 0 \\ 0 & 0 \\ k_{\omega} & 0 \\ 0 & k_{\omega} \\ g_{\lambda,r} & 0 \\ 0 & g_{\lambda,l} \\ 0 & 0 \\ 0 & 0 \\ 0 & 0 \\ 0 & 0 \end{bmatrix} \tag{4.24}$$

Thusly exhibiting the model Eqs. (4.24) - (4.24) is affine-in-the-control.

Remark 2: In this control-affine approximated model, the following parameters will need to be identified through experiments: shown in section (6)

CHAPTER 5

PARAMETER IDENTIFICATION

The parameters a_1, a_2 and b in the control affine model represent mechanical terrain characteristics and will vary in different terrains such as loamy soil and sand soil. Additionally, the parameters cannot be easily found by experimentation and/or calculation. For this reason, these parameters will be estimated online along with the robot velocities using an extended Kalman filter.

5.1 Process Model

The state variables to be estimated are

$$x = \begin{bmatrix} \dot{x}_R & \dot{y}_R & \dot{\psi}_R & \omega_r & \omega_l & a_1 & a_2 & b \end{bmatrix}^T \tag{5.1}$$

As compared with the state variable vector in Eq. (4.2), the slip/skid ratio and slip angle states are not included because they can be computed from the robot velocity states directly.

The process model is then

$$\boldsymbol{f}(\boldsymbol{x},\boldsymbol{u},\boldsymbol{w}) = \begin{bmatrix} \dot{\psi}_R\dot{y}_R + \frac{2a_1}{m}\left[sign(\lambda_l) + sign(\lambda_r) - e^{-a_2|\lambda_r|} - e^{-a_2|\lambda_l|}\right] \\ -\dot{\psi}_R\dot{x}_R + \frac{b}{m}\sum_{i=1}^{4}\beta_i \\ \frac{2Wa_1}{I}\left[sign(\lambda_l) - sign(\lambda_r) - e^{-a_2|\lambda_l|} + e^{-a_2|\lambda_r|}\right] + \frac{Lb}{I}\left[\beta_1 + \beta_2 - \beta_3 - \beta_4\right] \\ -k_\omega\omega_r \\ -k_\omega\omega_l \\ 0 \\ 0 \\ 0 \end{bmatrix} + \begin{bmatrix} w_1 \\ w_2 \\ w_3 \\ w_4 \\ w_5 \\ w_6 \\ w_7 \\ w_8 \end{bmatrix} \tag{5.2}$$

In this process model, $w_i$is assumed to be zero mean white Gaussian noise, with a covariance of Q.

$$w \sim (0, Q) \tag{5.3}$$

5.2 Measurement Model

Measurements are taken from an inertial measurement unit (IMU) and a quadrature wheel encoder for the right and left wheel velocities as

$$z = \begin{bmatrix} \ddot{x}_R & \ddot{y}_R & \dot{\psi}_R & \omega_r & \omega_l \end{bmatrix} \tag{5.4}$$

Here the acceleration measurement model is taken from the first two rows in Eq. (5.2), and the yaw rate and the left and right wheel bank angular rates can be directly ascertained from state estimate.

$$\boldsymbol{h}(\boldsymbol{x},\boldsymbol{v}) = \begin{bmatrix} \dot{\psi}_R \dot{y}_R + \frac{2a_1}{m}\left[sign(\lambda_l) + sign(\lambda_r) - e^{-a_2|\lambda_r|} - e^{-a_2|\lambda_l|}\right] \\ -\dot{\psi}_R \dot{x}_R + \frac{b}{m}\sum_{i=1}^{4}\beta_i \\ \dot{\psi}_R \\ \omega_r \\ \omega l \end{bmatrix} + \begin{bmatrix} v_1 \\ v_2 \\ v_3 \\ v_4 \\ v_5 \end{bmatrix} \tag{5.5}$$

The measurement noise, v_I , is also assumed as zero mean white Gaussian noise with a covariance of R.

$$v \sim (0, R) \tag{5.6}$$

5.3 Hybrid Extended Kalman Filter

In the hybrid extended Kalman filter (EKF) following [21], the prediction equation include

$$\dot{\hat{\boldsymbol{x}}}^{-} = \boldsymbol{f}\left(\hat{\boldsymbol{x}}^{+}, \boldsymbol{u}, \boldsymbol{0}\right) \tag{5.7}$$

In which $\hat{\boldsymbol{x}}^{-}$ and $\hat{\boldsymbol{x}}^{+}$ are the state estimate (apriori- and a-posteri+), and $\boldsymbol{f}$ is eq. (5.2) without process noise.The time update for the state covariance matrix $\boldsymbol{P}$ is predicted using

$$\dot{\boldsymbol{P}}^{-} = \boldsymbol{A}\boldsymbol{P}^{+} + \boldsymbol{P}^{+}\boldsymbol{A}^{\boldsymbol{T}} + \boldsymbol{L}\boldsymbol{Q}\boldsymbol{L}^{\boldsymbol{T}} \tag{5.8}$$

in which matrices A and L are calculated using

$$\boldsymbol{A} = \frac{\partial \boldsymbol{f}}{\partial \boldsymbol{x}}\Big|_{\hat{x}} \quad \boldsymbol{L} = \frac{\partial \boldsymbol{f}}{\partial \boldsymbol{w}}\Big|_{\hat{x}} \tag{5.9}$$

These two update equations (Eq. (5.7) and Eq. (5.8)) are performed with a numerical integration scheme, here a 4th order Runge-Kutta is used.

The Kalman gain at time step k is then computed using the time update error covariance prediction are

$$\boldsymbol{K_k} = \boldsymbol{P_k^{-}}\boldsymbol{H_k^{T}}\left[\boldsymbol{H_k}\boldsymbol{P_k^{-}}\boldsymbol{H_k^{T}} + \boldsymbol{M_k}\boldsymbol{R_k^{-}}\boldsymbol{M_k^{T}}\right]^{-1} \tag{5.10}$$

And the Joseph stabilized error covariance measurement update equation is used to find the error covariance matrix at time step k

$$\boldsymbol{P}_k^{+} = \left(\boldsymbol{I} - \boldsymbol{K}_k\boldsymbol{H}_k\right)\boldsymbol{P}_k^{-}\left(\boldsymbol{I} - \boldsymbol{K}_k\boldsymbol{H}_k\right) + \boldsymbol{K}_k\boldsymbol{M}_k\boldsymbol{R}_k\boldsymbol{M}_k^{T}\boldsymbol{K}_k^{T} \tag{5.11}$$

The state estimate measurement update (posteri+) is

$$\hat{\boldsymbol{x}}_k^{+} = \hat{\boldsymbol{x}}_k^{-} + \boldsymbol{K}_k\left(\boldsymbol{y}_k - \boldsymbol{H}_k\hat{x}_k^{-}\right) \tag{5.12}$$

Here matrices $\boldsymbol{H}$ and $\boldsymbol{M}$ are the process model and measurement model jacobians defined as

$$\boldsymbol{H} = \frac{\partial \boldsymbol{h}}{\partial \boldsymbol{x}}\Big|_{\hat{x}} \quad \boldsymbol{M} = \frac{\partial \boldsymbol{h}}{\partial \boldsymbol{v}}\Big|_{\hat{x}} \tag{5.13}$$

CHAPTER 6

SIMULATIONS AND EXPERIMENTS

To validate the proposed approximate WTIM and EKF estimation scheme, simulations and experiments of turning maneuvers were conducted. In both situations a data set of the robot dynamics was acquired and the EKF was run ad-hoc. The terramechanic WTIM was used for the simulated data set and a custom robot (DDAGR) designed for scouting of commercial strawberry orchards was utilized for the actual data set.

6.1 Simulation

Before testing the model and estimation scheme on real components the terramechanic WTIM was employed for the acquisition of a simulated accurate data set of the robot dynamics. Terramechanic parameters are generally found experimentally with a Bevameter, however because Bevameter are costly and the focus of this research was not terramechanic the parameters used for the simulation were taken from [17] and are tabulated in the appendix. These parameters are meant to simulate off road environments in sandy loam which

has similar properties to strawberry orchards in temperate environments, such as those found in Northern California and Oregon.

To conduct the simulation, the physical characteristics of DDAGR where used in the skid-steer model and EKF.

Table 6.1: DDAGR physical properties

Parameter	Value	Unit	Description
m	168	kg	Robot Mass
I	100	$kg \cdot m^2$	Moment Of Inertia
r	28	cm	Wheel Radius
W	58	cm	Half of Robot Width
L	33	cm	Half of Robot Length

Additionally, a small amount of measurement noise and process noise was added to the simulation data using MATLABs Gaussian pseudo random number generator *randn*. To initialize the EKF the following initial error, process noise and measurement noise covariance matrices were used.

$$\begin{aligned} \boldsymbol{P_0} &= diag\left(\begin{bmatrix} 0 & 0 & 0 & 0 & 0 & 1 & 0.25 & 1 \end{bmatrix}\right) \\ \boldsymbol{Q} &= diag\left(\begin{bmatrix} 500 & 500 & 500 & 0 & 0 & 1 & 0.01 & 1 \end{bmatrix} 1e-5\right) \\ \boldsymbol{R} &= diag\left(\begin{bmatrix} 5000 & 5000 & 5000 & 1 & 1 \end{bmatrix} 1e-5\right) \end{aligned} \tag{6.1}$$

To acquire the data set for a cross-the-bed like turning maneuver the wheel speeds were varied at three points in time the wheel bank speeds are tabulated below

Table 6.2: Wheel bank velocities used for simulation

$t[s]$	$\omega_r[\frac{rad}{s}]$	$\omega_l[\frac{rad}{s}]$
0.0-5.0	0.701	0.701
5.0-22.5	0.0	1.195
22.5-25.0	0.701	0.701

Below the robot trajectory, all eight estimated states, eq. (5.1), and the EKF covariance trace value are shown. The trajectory is found by integrating the robot velocities and is shown to clarify the maneuver being done. The simulated wheel bank velocities are identical to the estimated wheel bank velocities because the model used for each bank is identical, namely $\dot{\omega} = k_\omega (\omega_c - \omega)$ where $k_\omega = 4.5$

The approximate WTIM parameters estimated by the EKF.

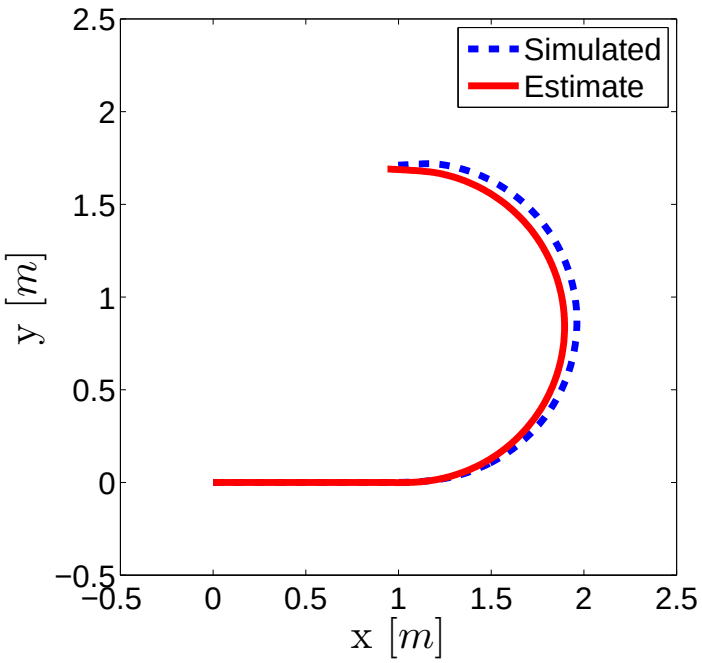

Figure 6.1: Robot Trajectory for the Simulation

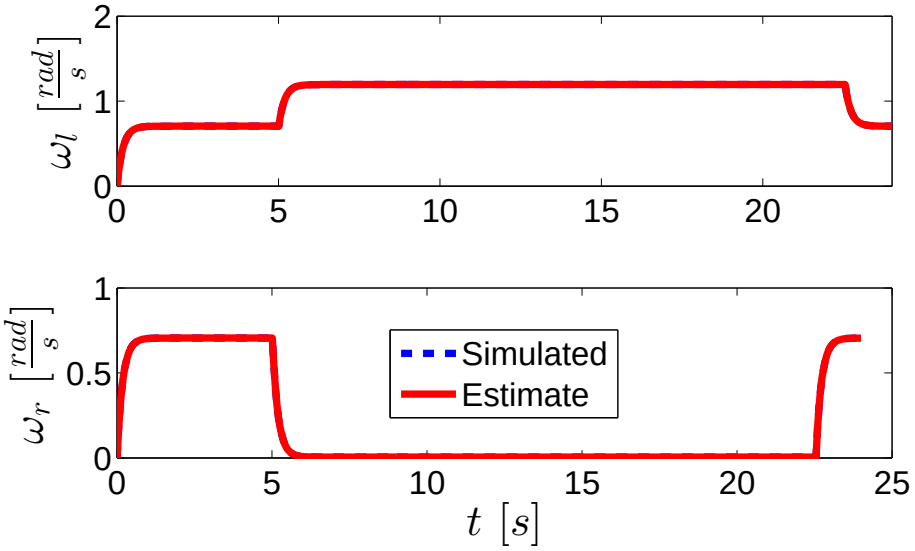

Figure 6.2: Simulated Wheel Bank Angular Velocities (ω_r and ω_l)

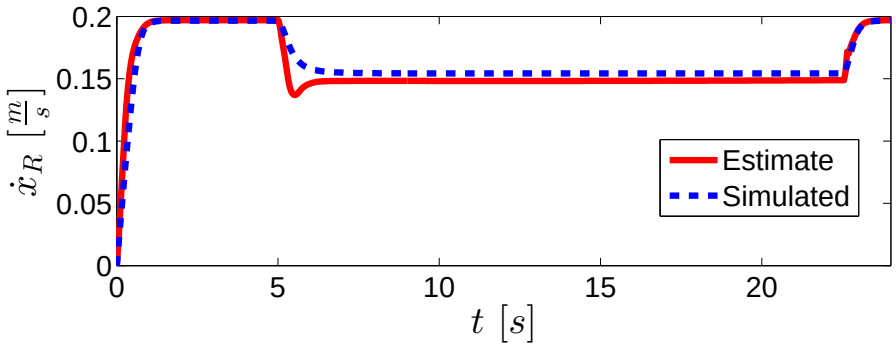

Figure 6.3: Longitudinal Velocity ($\dot{x}_R$) During Simulation

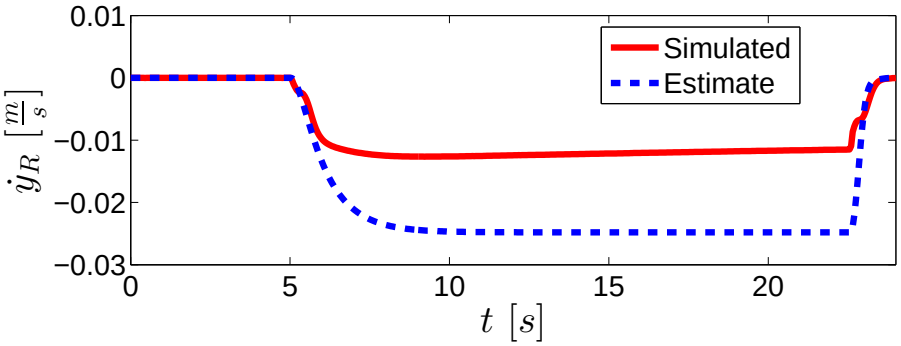

Figure 6.4: Lateral Velocity ($\dot{y}_R$) During Simulation

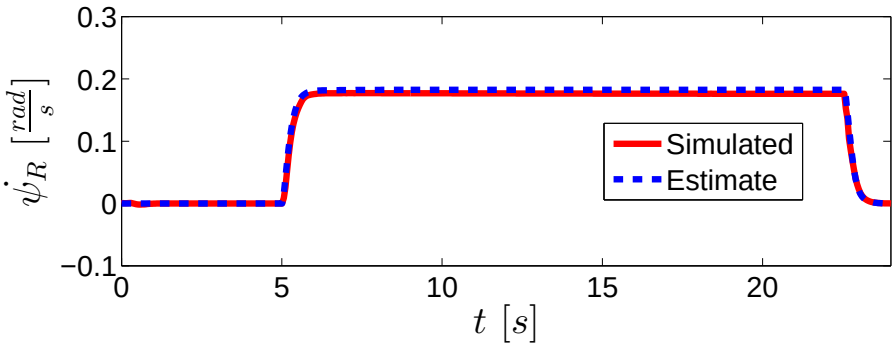

Figure 6.5: Yaw Rate ($\dot{\psi}_R$) During Simulation

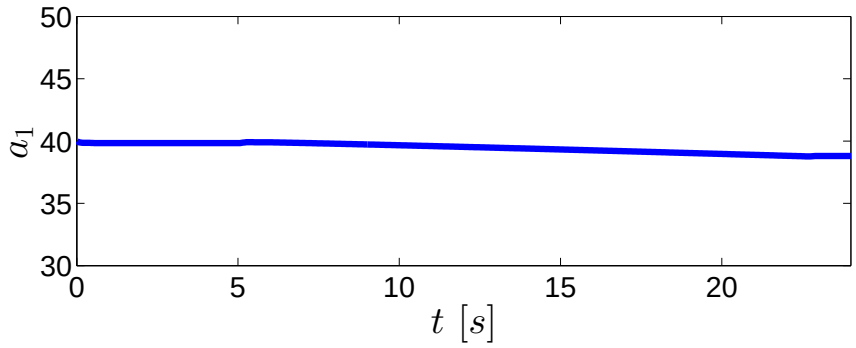

Figure 6.6: a_1 Parameter Estimate During Simulation

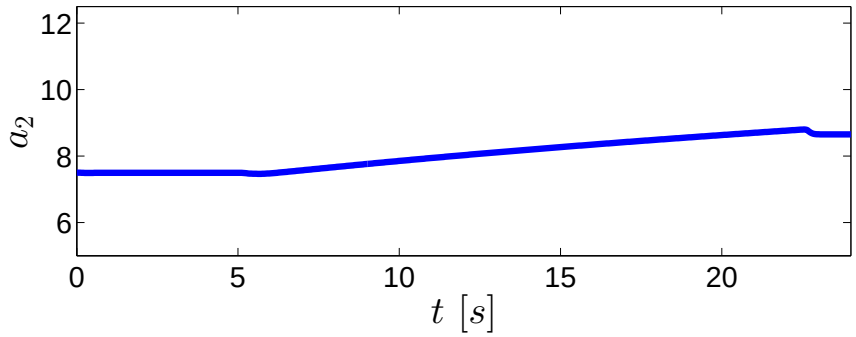

Figure 6.7: a_2 Parameter Estimate During Simulation

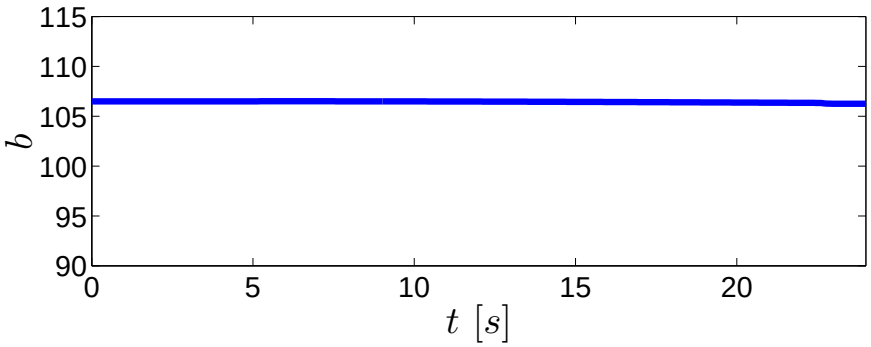

Figure 6.8: b Parameter Estimate During Simulation

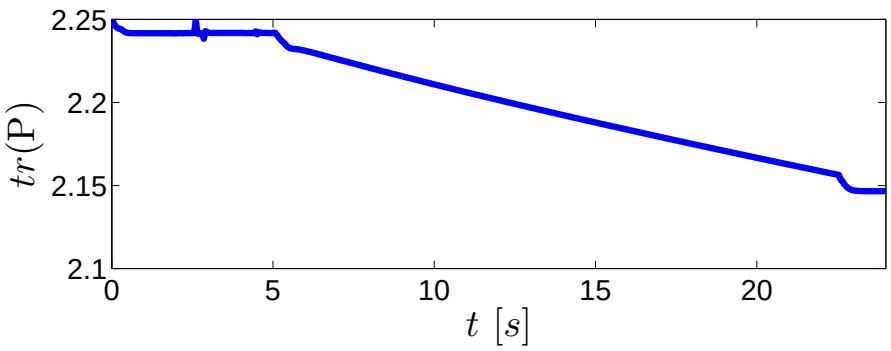

Figure 6.9: Trace of Error Covariance Matrix ($\mathbf{tr}\,[P]$) During Simulation

6.2 Experiment

A brief description of the robotic strawberry orchard platform, DDAGR,is given. For locomotion DDAGR is equipped with two 24 Volt DC wheelchair motors. For navigation DDAGR is equipped with an array of onboard sensors which include, but are not limited to, an*InvenSense MPU 6050* and two *US Digital E3* optical quadrature encoders. The control system which was developed at the University of Central Floridas Arc-Lab, has a two level hierarchy. The first level consists of an *Arduino Mega 2560* in conjunction with a *SuperDroid Encoder Buffer* and a *Dimension engineering Sabertooth 2x60 amp voltage regulator*. The software uploaded onto the *Arduino* accomplishes three tasks: PID regulation of the wheel shaft angular velocity, orientation estimation of the robot and data acquisition for the second highest level control system. For satisfactory results the wheel shaft angular velocity control laws and orientation estimation scheme have a 1 kHz update rate whereas raw sensor samples are streamed from the data acquisition portion of the software at around

125 Hz. The IMU is placed at the robot center of mass namely $(x_R, y_R) = (0, 0)$ and the optical encoders are placed on the rotor shaft of each of the two 24 Volt DC motors.

Figure 6.10: DDAGR In Front of a strawberry bed in *Pappy's Patch* Strawberry orchard

For experimental validation DDAGR was brought to *Pappys patch* a local u-pick strawberry patch near the UCF campus. The physical characteristics of DDAGR used in the EKF are tabulated in table 6.1. To approximate the measurement noise of the IMU a static data set was taken while the robot remained stationary. To approximate the measurement noise of the optical encoders the DC motors underwent a step input while on raised blocks so that no external disturbances might affect the steady state data. The process noise and initial error covariance was found through trial and error.

Table 6.3: Wheel bank velocities used for simulation

$t[s]$	$\omega_r[\frac{rad}{s}]$	$\omega_l[\frac{rad}{s}]$
2.0-18.0	0.716	0.716
18.0-38.0	0.36	1.074

the initial error, process noise and measurement noise covariance matrices used for the experimental EKF are

$$\begin{aligned} \boldsymbol{P_0} &= diag\left(\begin{bmatrix} 0 & 0 & 0 & 0 & 0 & 1 & 0.01 & 1 \end{bmatrix}\right) \\ \boldsymbol{Q} &= diag\left(\begin{bmatrix} 10 & 100 & 10 & 0 & 0 & 1 & 0.01 & 1 \end{bmatrix} 1e-7\right) \\ \boldsymbol{R} &= diag\left(\begin{bmatrix} 0.5 & 0.5 & 0.007 & 10 & 10 \end{bmatrix} 1e-2\right) \end{aligned} \tag{6.2}$$

During the experimental validation the horizontal plane assumption is violated and the gravitational inertial effects cannot be neglected. The following longitudinal and lateral acceleration dynamics listed in eq. 10 must be altered to account for the gravitational effects due to slight variations in the orientation of the robot. In the experiments conducted *FreeIMU*, an open source, orientation estimator was used to keep track of the traditional Z-Y-X Euler angle. Using a Z-Y-X rotation matrix the dynamics listed in equation (2.10) become

$$\ddot{x}_R = \dot{\psi}_R \dot{y}_R - g sin\,(\theta) + \sum F_{ext,x}/m$$
$$\ddot{y}_R = -\dot{\psi}_R \dot{x}_R + g sin\,(\phi)\, cos\,(\theta) + \sum F_{ext,x}/m \tag{6.3}$$
$$\ddot{\psi}_R = \sum M_{ext}/I$$

Where θ is the Euler angle about the y-axis, ϕ is the Euler angle about the x-axis and g is the gravitational constant. Note equation (6.3) affects both the process model (5.2) and the measurement model (5.5).

Below all eight estimated states (5.1) and the EKF covariance trace value are shown. For safety during the experiment, the PID gain values of the motor wheel shaft velocity controllers where tuned to give a slower response then used in the simulation. The motor gain value was appropriately changed to match the slower response time, in other words $k_\omega = 1.4$

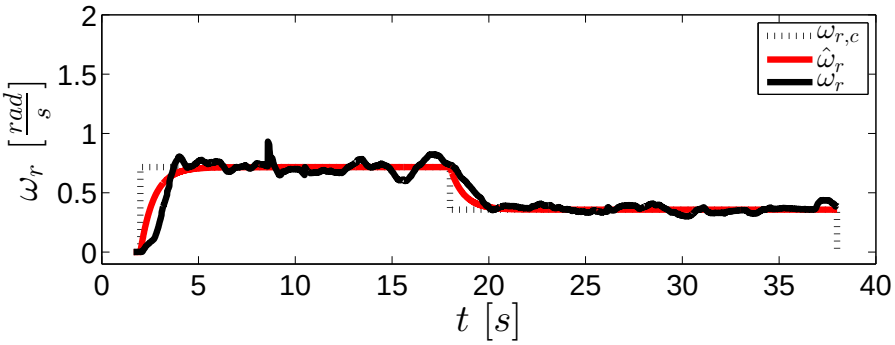

Figure 6.11: Right Wheel Bank Angular Velocity (ω_r) During Experiment

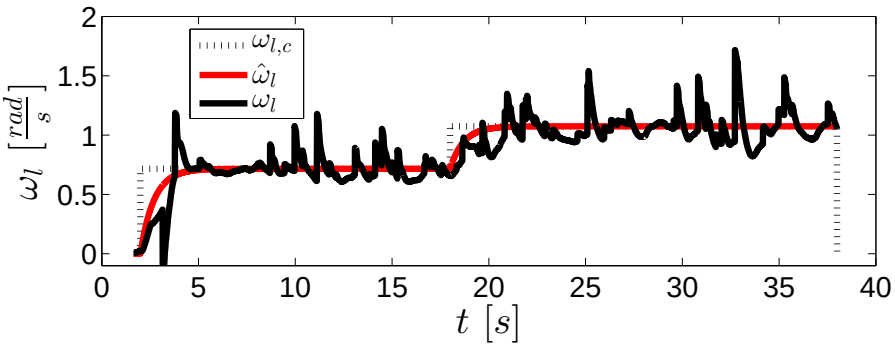

Figure 6.12: Left Wheel Bank Angular Velocity (ω_l) During Experiment

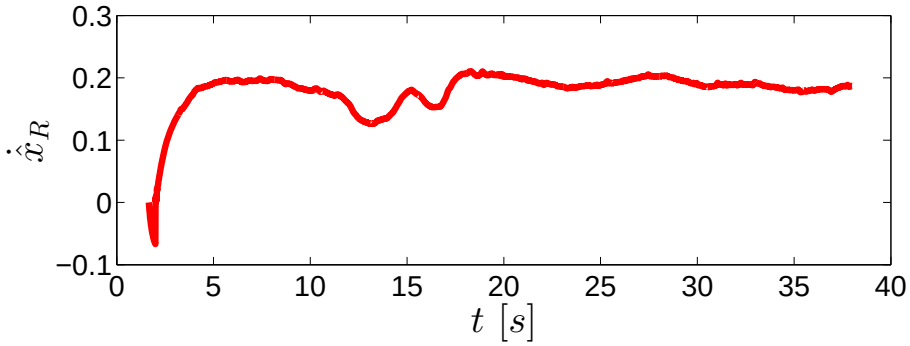

Figure 6.13: Longitudinal Velocity ($\dot{x}_R$) During Experiment

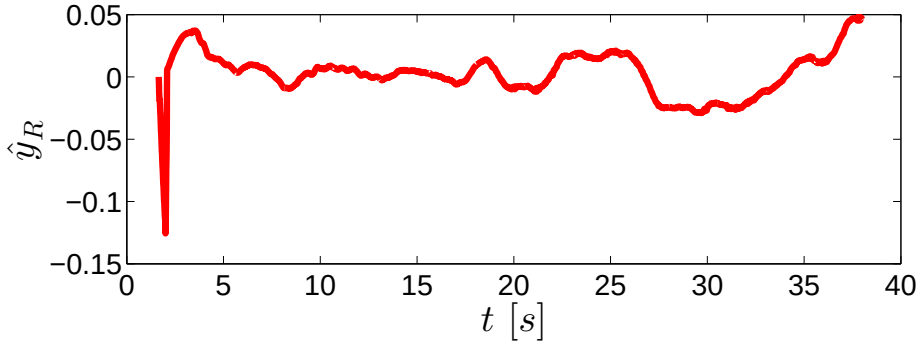

Figure 6.14: Lateral Velocity ($\dot{y}_R$) During Experiment

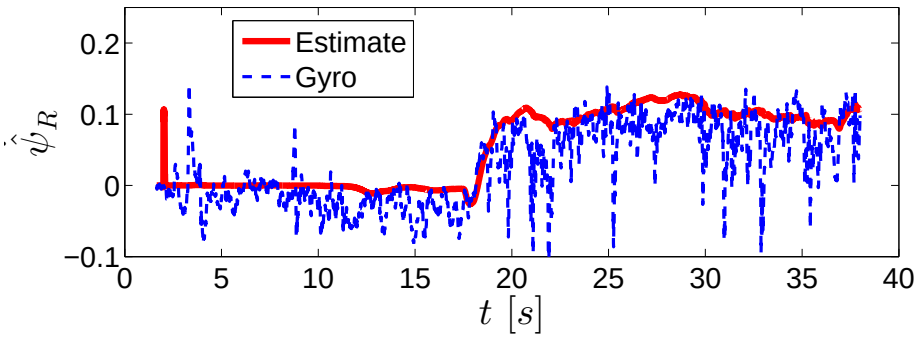

Figure 6.15: Yaw Rate ($\dot{\psi}_R$) During Experiment

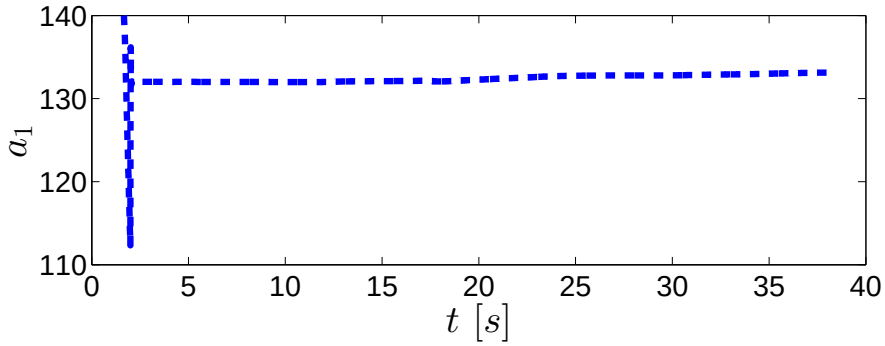

Figure 6.16: a_1 Parameter Estimate During Experiment

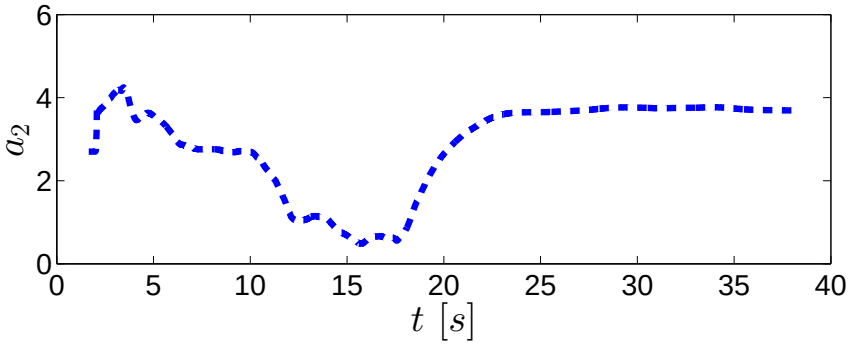

Figure 6.17: a_2 Parameter Estimate During Experiment

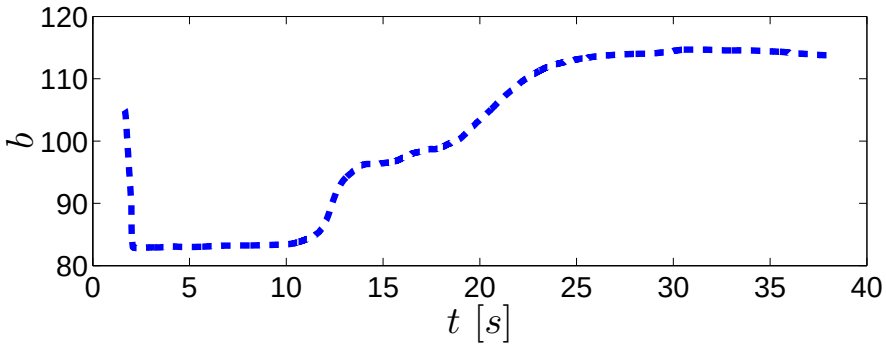

Figure 6.18: b Parameter Estimate During Experiment

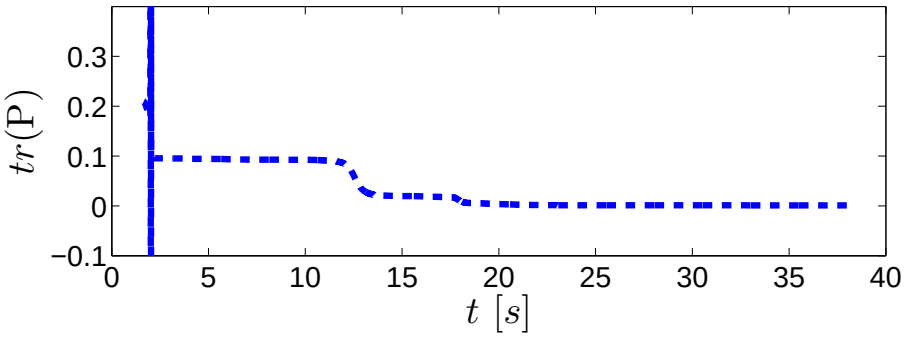

Figure 6.19: Trace of Error Covariance Matrix ($\mathbf{tr}\,[P]$) Estimate During Experiment

6.3 Results

The terramechanic parameters used in the turn maneuver simulation are meant to simulate off road environments in sandy loam which has similar properties to strawberry orchards in temperate environments, such as those found in Northern California and Oregon. In Florida strawberry orchards have drier looser sand and thus the results differ greatly from the simulation and the experiment. The shrinking error covariance matrix trace and estimated parameter convergence however are signs that the model and estimation scheme is valid.

CHAPTER 7

CONCLUSION

In this paper we have proposed two wheel terrain interaction models. The first model is the application of the Terramechanic technique to wheels of the torus geometry, which can be used for high fidelity simulations of wheeled mobile robots in soft terrain. The second model is an approximate wheel terrain interaction model which was shown to be useful for control applications. The approximate model was used to construct an affine in the control model for a skid steer wheeled mobile robot in loose sand. Furthermore, we have experimentally validated the model and proposed an online parameter identification scheme for the unknown model parameters. The estimation scheme requires only an IMU and optical encoders which are readily and cheaply available.

APPENDIX: A

TERRAMECHANICS

A.1 Integral Bounds

For the clarity and completeness of the study, the brief derivation of the terramechanic pressure equations from [13] and [12] are listed here.

First relationships relating the integral bounds θ_f and θ_r to the sinkage depth N_z are established for a wheel rolling horizontally on a plane. The entry angle θ_f can be computed using

$$\theta_f = cos^{-1}\left(1 - \left[N_z / \left(c + a\right)\right]\right) \tag{A.1}$$

and the exit angle θ_r is

$$\theta_r = \theta_f \lambda_\theta \tag{A.2}$$

in which λ_θ is the terrain compressibility ratio.

The right and left bound angle ψ_r and ψ_l

$$\psi_l = cos^{-1}\left(1 - N_z/a\right) \tag{A.3}$$

$$\psi_r = -\psi_l \tag{A.4}$$

The sinkage depth N_z in the above equations is solved for using the search algorithm shown in Appendix B.

A.2 Normal Stress

The normal stress equation used in the model is

$$\sigma(\theta, \psi) = \left(\frac{k_c}{b_\psi} + k_\phi\right) r_\psi^n \bar{\theta}^n \tag{A.5}$$

in which k_c is the cohesion factor and k_ϕ is the angle of cohesion factor. The term $r_\psi \bar{\theta}$ represent the effective location along the wheel. The the radius of a vertical wheel slice, r_ψ can be found using

$$r_\psi = c + acos\,(\psi) \tag{A.6}$$

The modified angle $\bar{\theta}$ is defined as

$$\bar{\theta} = \begin{cases} \cos(\theta) - \cos(\theta_f), & \theta_m \leq \theta < \theta_f \\ \cos\left[\theta_f - \left(\frac{\theta - \theta_r}{\theta_m - \theta_r}\right)(\theta_f - \theta_m)\right] - \cos(\theta_f), & \theta_r < \theta \leq \theta_m \end{cases} \tag{A.7}$$

in which θ_m is the point of max radial stress and is specified by the terrain properties a_0 and a_1 in the equation

$$\theta_m = (a_0 + a_1 \lambda)\,\theta_f \tag{A.8}$$

Where λ is the wheel slip ratio. In Eq. (A.5), b_ψ is the effective width of the tire at point on the surface which can be found like so

$$b_\psi = 2bsin\,(\psi) \tag{A.9}$$

A.3 Shear Stress

The shear stress along the contact patch is primarily a function of the shear deformation j the wheel has done on the terrain and the normal stress σ the wheel imparts on the terrain.

$$\tau(\sigma, j) = \tau_m \left(1 - e^{-j/K}\right) \tag{A.10}$$

where j is the shear deformation of the terrain along the contact patch and is the magnitude of the shear deformation vector, namely $j = |\boldsymbol{j}| = \sqrt{j_l^2 + j_t^2}$. Note that j_t is the tangent deformation, j_l is the lateral deformation and the normal deformation j_n is assumed to be zero. The lateral and shear deformations will be derived later in this appendix. K is the shear modulus, a constant terrain property parameter, and τ_m is the maximum shear stress which is a function of the normal stress and can be computed by

$$\tau_m = c_m + \sigma tan(\phi) \tag{A.11}$$

which is dictated by the terrain cohesion property c_m and the terrain angle cohesion property ϕ.

The shearing stress in Eq. (A.10) is broken into the lateral and tangential components using the approach in [13], where the shearing velocity vector, $\begin{bmatrix} v_{jt} & v_{jl} & v_{jn} \end{bmatrix}^T$, is utilized to separate the tangential and lateral components as (the positive orientation of the shear stress is the same as in figure 3.1)

$$\tau_t(\sigma, j) = \tau_t(\sigma, j) \frac{-v_{jt}}{\sqrt{v_{jt}^2 + v_{jl}^2 +}} \tag{A.12}$$

and

$$\tau_t(\sigma, j) = \tau_t(\sigma, j) \frac{-v_{jl}}{\sqrt{v_{jt}^2 + v_{jl}^2 +}} \tag{A.13}$$

The positive directions for the shear velocity/ displacement are shown in the figure below.

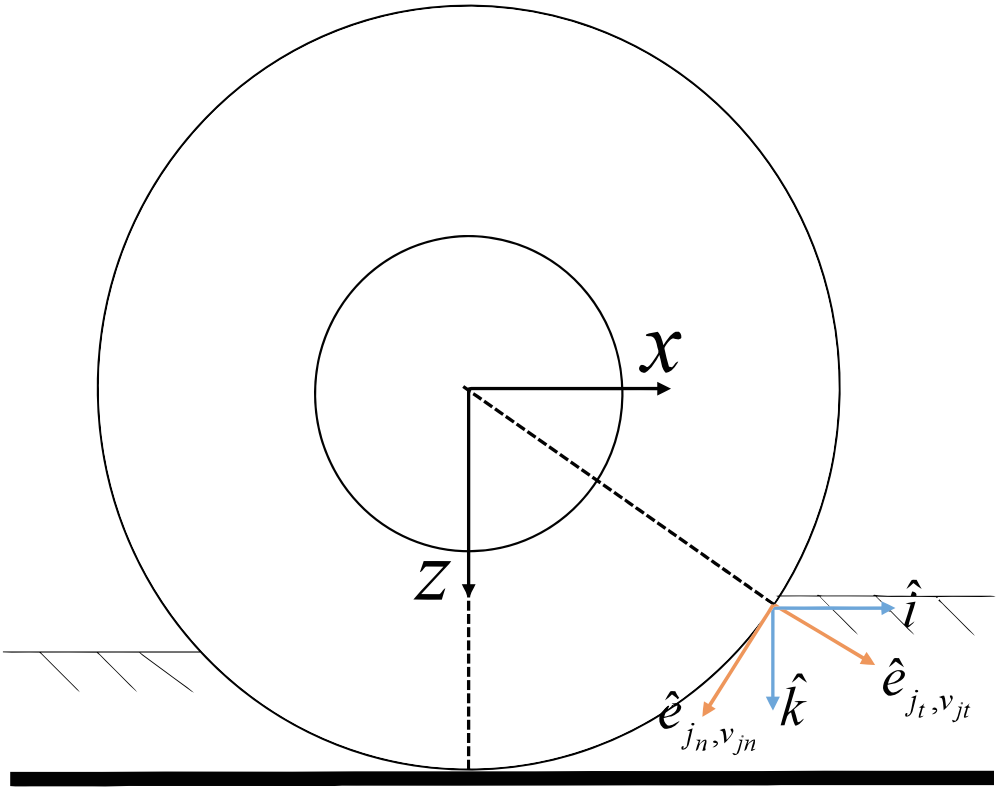

Figure A.1: Positive Shear Deformation Orientation

The shear velocities of the wheel surface $\begin{bmatrix} v_{jt} & v_{jl} & v_{jn} \end{bmatrix}^T$ are the lateral and tangential components of the absolute wheel velocity at any point along the wheel surface. The velocity components in the hub axis world frame can be expressed as

$$\boldsymbol{V}\left(\boldsymbol{\theta},\boldsymbol{\psi}\right)=\boldsymbol{V}^{H}+\boldsymbol{\omega}^{H}\times\boldsymbol{r} \tag{A.14}$$

where $\boldsymbol{V}^{H}$ and $\boldsymbol{\omega}^{H}$ are the linear and angular velocities of the wheel axle hub and $\boldsymbol{r}$ is the position vector discussed in Eq. (3.1). A suitable rotation matrix from the hub to the shear velocity/displacement coordinate system (shown in the figure above) can be found by pre multiplying Eq. (3.7) with a half revolution rotation in the normal-axis (z axis):

$$R^{*}=\begin{bmatrix}-1 & 0 & 0\\ 0 & -1 & 0\\ 0 & 0 & 1\end{bmatrix} \tag{A.15}$$

Thus the shearing velocity is

$$\boldsymbol{V}\left(\theta,\psi\right)=R^{*}\boldsymbol{V} \tag{A.16}$$

Carrying out the arithmetic in Eqs. (A.14) and(A.16) leads to the following relations for the tangential and lateral shearing rates as

$$\begin{aligned}v_{jt}\left(\theta,\psi\right)=&-\left[v_{x}-\omega_{z}y+\omega_{y}z\right]\cos\left(\theta\right)\\ &-\left[v_{y}+\omega_{z}x-\omega_{x}z\right]\sin\left(\psi\right)\cos\left(\theta\right)\\ &+\left[v_{z}-\omega_{y}x+\omega_{x}y\right]\cos\left(\psi\right)\cos\left(\theta\right)\end{aligned} \tag{A.17}$$

and

$$\begin{aligned} v_{jl}(\theta,\psi) = &-[v_y + \omega_z x - \omega_x z]\cos(\psi) \\ &-[v_z - \omega_y x + \omega_x y]\sin(\psi) \end{aligned} \tag{A.18}$$

where the variables x, y and z come from the position vector:

$$\begin{Bmatrix} x \\ y \\ z \end{Bmatrix} = \boldsymbol{r}(\theta,\psi) = \begin{Bmatrix} (c + a\cos(\psi))\sin(\theta) \\ b\sin(\psi) \\ (c + a\cos(\psi))\cos(\theta) \end{Bmatrix} \tag{A.19}$$

The shear deformation of the terrain j that has occurred at a point along the wheel terrain contact patch can be calculated by integrating the shear rate over time. In Terramechanic WTIM models a quasi-steady state rolling on horizontal ground is assumed. Hence the velocity $\boldsymbol{V}^H$ and the angular rate $\boldsymbol{\omega}^H$ at the wheel hub are treated as constants. Then the shear deformation of the terrain j in the lateral and tangential directions can be calculated using [16]

$$j_l = \int_0^t v_{jl} dt = \int_\theta^{\theta_f} v_{jl} \frac{d\theta}{\omega_y} \tag{A.20}$$

$$j_t = \int_0^t v_{jt} dt = \int_\theta^{\theta_f} v_{jt} \frac{d\theta}{\omega_y} \tag{A.21}$$

Carrying out the integration leads to the following relationships.

$$j_t(\theta,\psi)=\frac{1}{\omega_y}\left\{\begin{array}{l} A_{jt}\left[\sin\theta_f-\sin\theta\right] \\ +C_{jt}\left[\cos^2\theta_f-\cos^2\theta\right]/2 \\ +B_{jt}[\theta_f+\sin\theta_f\cos\theta_f-\theta-\sin\theta\cos\theta]/2 \\ +D_{jt}[\theta_f-\sin\theta_f\cos\theta_f-\theta+\sin\theta\cos\theta]/2 \\ +E_{jt}\left[\cos^2\theta_f-\cos^2\theta\right]/2 \end{array}\right\} \tag{A.22}$$

$$j_l(\theta,\psi)=\frac{1}{\omega_y}\left\{\begin{array}{l} A_{jl}\left(\theta_f-\theta\right) \\ +B_{jl}\left(\cos\theta-\cos\theta_f\right)-C_{jl}\left(\sin\theta_f-\sin\theta\right) \end{array}\right\} \tag{A.23}$$

$$\begin{aligned} A_{jt}&=-v_x+\omega_z b\sin\psi \\ B_{jt}&=-\omega_y\left(c+a\cos\psi\right) \\ C_{jt}&=-v_y\sin\psi+v_z\cos\psi+\omega_x b\sin\psi\cos\psi \\ D_{jt}&=-\omega_z\left(c+a\cos\psi\right)\sin\psi-\omega_y\left(c+a\cos\psi\right)\cos\psi \\ E_{jt}&=\omega_x\left(c+a\cos\psi\right)\sin\psi \end{aligned} \tag{A.24}$$

$$\begin{aligned} A_{jl}&=-v_y\cos\psi-v_z\sin\psi-\omega_x b\sin^2\psi \\ B_{jl}&=-\omega_z\left(c+a\cos\psi\right)\cos\psi+\omega_y\left(c+a\cos\psi\right)\sin\psi \\ C_{jl}&=\omega_x\left(c+a\cos\psi\right)\cos\psi \end{aligned} \tag{A.25}$$

A.4 Wheel Sinkage Depth Search Algorithm

All the variables for the terramechanic WTIM integral have been expressed in terms of the angles (θ, ψ). The wheel kinematics, terrain property coefficients, and wheel geometry constants must be known prior to integrating the stress along the contact patch. These variables can be measured, produced by a simulation or treated as design variables. The sinkage depth however is unknown and is searched for by the Terramechanic WTIM algorithm [16]. To search for the sinkage depth an initial guess is taken, usually we start assuming the wheel has not sunk into the dirt at all. The algorithm then evaluates the force component normal to the terrain surface and compares that with the wheel load. If the terramechanic model indicates the terrain reaction force is equal but opposite to the wheel load then the sinkage depth has been found, otherwise a numerical searching method is used to increment the sinkage depth and try again, this process is repeated until the correct depth is found. For this model the integral is solved numerically with a double Gaussian quadrature and the VanWijngaarden-Dekker-Brent search method is used to find the sinkage depth [22]. The Terramechanic WTIM was realized in C source code and and compiled as a mex (MATLAB executable) program for use in the MATLAB and Simulink simulation environments.

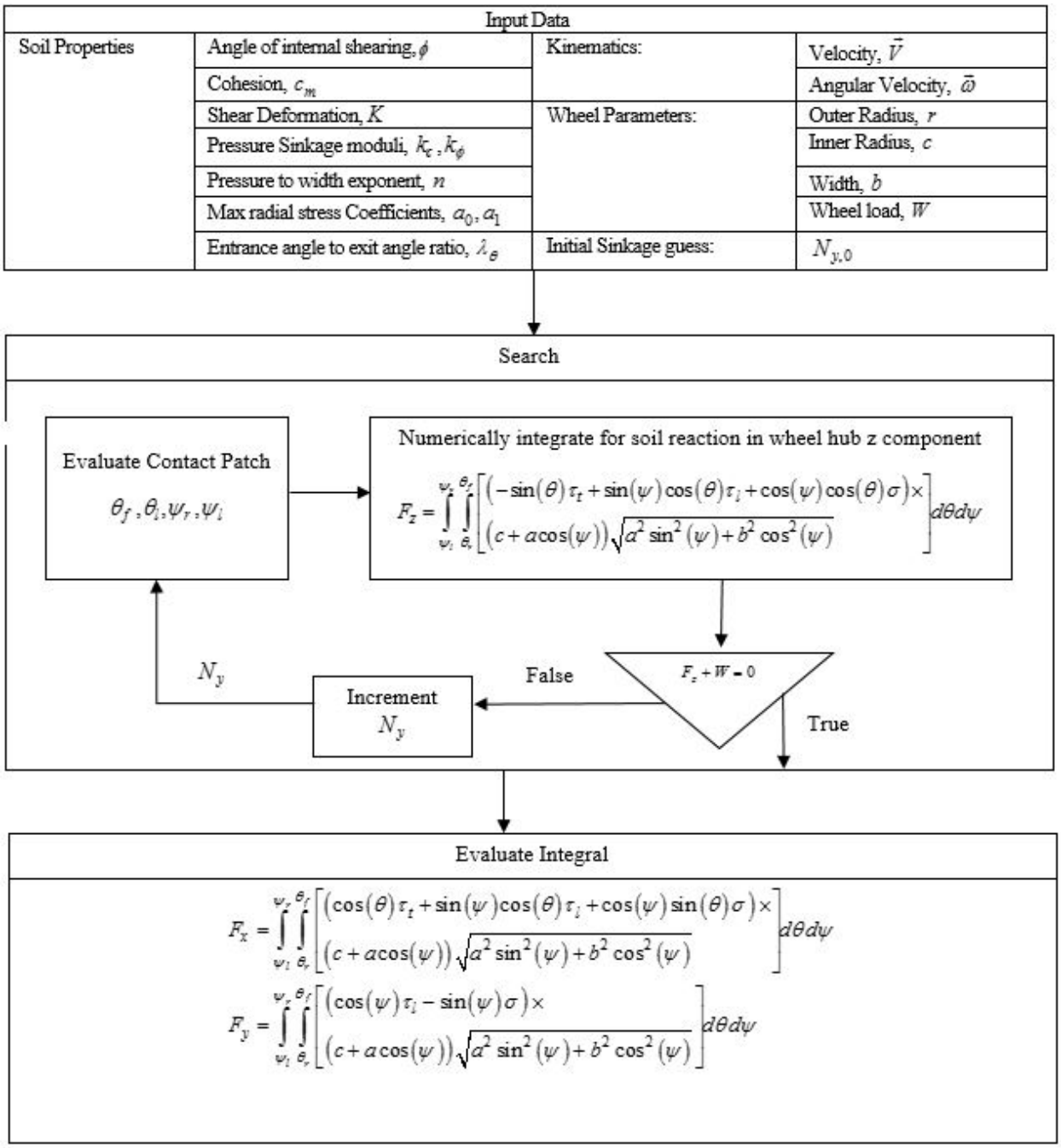

Figure A.2: Terramechanic WTIM Algorithm

A.5 Table

Table A.1: Terramechanic WTIM parameter description and values

Parameter	Value	Unit	Description
a	22.94	cm	Major Radius
$2b$	20.32	cm	Wheel Width
c	5.0	cm	Minor Radius
c_m	4140	Pa	Cohesion Coefficient
ϕ	13	deg	Internal Friction Angle
n	0.5	–	Sinkage Exponent
k_c	13,190	N/m^{n+1}	Cohesive Modulus
k_ϕ	692,000	N/m^{n+1}	Friction Modulus
K	0.006	m	Shear Modulus
a_0	0.5	–	Coefficient for θ_m
a_1	0.5	–	Coefficient for θ_m
λ_θ	0.9	–	Coefficient for θ_r

APPENDIX: B

PARAMETER IDENTIFICATION JACOBIANS

B.1 Slip/Skid Ratio Partial Derivatives

The partial derivatives of the state equation require the partial for the absolute value of the slip/skid ratio we begin with equation (4.3)

$$\lambda_j = \begin{cases} [(c+a)\,\omega_j - \dot{x}_j]/(c+a)\,\omega_j \;, |\dot{x}_j| \leq |(c+a)\,\omega_j| \\ \\ \quad [(c+a)\,\omega_j - \dot{x}_j]/\dot{x}_j \;, |\dot{x}_j| > |(c+a)\,\omega_j| \end{cases}, j = r, l \tag{B.1}$$

We now take the partial derivative with respect to the parameter identification scheme states (5.1).

$$\frac{\partial\,|\lambda_l|}{\partial \dot{x}_R} = \begin{cases} \frac{-(c+a)\omega_l + W\dot{\psi}_R + \dot{x}_R}{[(c+a)\omega_l]^2 |\lambda_l|}, & slip \\ \frac{(c+a)\omega_l\left[-(c+a)\omega_l + W\dot{\psi}_R + \dot{x}_R\right]}{\left[W\dot{\psi}_R + \dot{x}_R\right]^3 |\lambda_l|}, & skid \end{cases} \tag{B.2}$$

$$\frac{\partial\,|\lambda_l|}{\partial \dot{\psi}_R} = \begin{cases} \frac{W\left[-(c+a)\omega_l + W\dot{\psi}_R + \dot{x}_R\right]}{[(c+a)\omega_l]^2 |\lambda_l|}, & slip \\ \frac{(c+a)\omega_l W\left[-(c+a)\omega_l + W\dot{\psi}_R + \dot{x}_R\right]}{\left[W\dot{\psi}_R + \dot{x}_R\right]^3 |\lambda_l|}, & skid \end{cases} \tag{B.3}$$

$$\frac{\partial\,|\lambda_l|}{\partial \omega_l} = \begin{cases} \frac{\left(\dot{x}_R + W\dot{\psi}_R\right)\left[(c+a)\omega_l - W\dot{\psi}_R - \dot{x}_R\right]}{(c+a)^2 \omega_l^3 |\lambda_l|}, & slip \\ \frac{(c+a)\left[(c+a)\omega_l - W\dot{\psi}_R - \dot{x}_R\right]}{\left[W\dot{\psi}_R + \dot{x}_R\right]^2 |\lambda_l|}, & skid \end{cases} \tag{B.4}$$

$$\frac{\partial\,|\lambda_r|}{\partial \dot{x}_R} = \begin{cases} \frac{-(c+a)\omega_r - W\dot{\psi}_R + \dot{x}_R}{[(c+a)\omega_l]^2 |\lambda_r|}, & slip \\ \frac{(c+a)\omega_r\left[-(c+a)\omega_r - W\dot{\psi}_R + \dot{x}_R\right]}{\left[W\dot{\psi}_R + \dot{x}_R\right]^3 |\lambda_r|}, & skid \end{cases} \tag{B.5}$$

$$\frac{\partial\,|\lambda_r|}{\partial \dot{\psi}_R} = \begin{cases} \frac{W\left[(c+a)\omega_r + W\dot{\psi}_R - \dot{x}_R\right]}{[(c+a)\omega_r]^2 |\lambda_r|}, & slip \\ \frac{(c+a)\omega_r W\left[(c+a)\omega_r + W\dot{\psi}_R - \dot{x}_R\right]}{\left[-W\dot{\psi}_R + \dot{x}_R\right]^3 |\lambda_r|}, & skid \end{cases} \tag{B.6}$$

$$\frac{\partial |\lambda_r|}{\partial \omega_r} = \begin{cases} \frac{\left(\dot{x}_R - W\dot{\psi}_R\right)\left[(c+a)\omega_r + W\dot{\psi}_R - \dot{x}_R\right]}{(c+a)^2\omega_r^3|\lambda_r|}, & slip \\ \frac{(c+a)\left[(c+a)\omega_r + W\dot{\psi}_R - \dot{x}_R\right]}{\left[W\dot{\psi}_R + \dot{x}_R\right]^2|\lambda_r|}, & skid \end{cases} \tag{B.7}$$

B.2 Process Model Jacobian

$$\boldsymbol{A} = \left.\frac{\partial \boldsymbol{f}}{\partial \boldsymbol{x}}\right|_{\hat{\boldsymbol{x}}} = \left.\begin{bmatrix} \frac{\partial \boldsymbol{f}_1}{\partial \boldsymbol{x}_1} & \cdots & \frac{\partial \boldsymbol{f}_1}{\partial \boldsymbol{x}_8} \\ \vdots & \ddots & \vdots \\ \frac{\partial \boldsymbol{f}_8}{\partial \boldsymbol{x}_1} & \cdots & \frac{\partial \boldsymbol{f}_8}{\partial \boldsymbol{x}_8} \end{bmatrix}\right|_{\hat{\boldsymbol{x}}} \tag{B.8}$$

B.2.1 Partial Derivatives for First State

$$\boldsymbol{f}_1 = \dot{\psi}_R \dot{y}_R + \frac{2a_1}{m}\left[sign\left(\lambda_l\right) + sign\left(\lambda_r\right) - \exp\left(-a_2\left|\lambda_l\right|\right) - \exp\left(-a_2\left|\lambda_r\right|\right)\right] \tag{B.9}$$

$$\left.\frac{\partial \boldsymbol{f}_1}{\partial \boldsymbol{x}_1}\right|_{\hat{\boldsymbol{x}}} = \left.\frac{\partial \boldsymbol{f}_1}{\partial \dot{x}_R}\right|_{\hat{\boldsymbol{x}}} = \frac{2a_1a_2}{m}\left[\frac{\partial |\lambda_l|}{\partial \dot{x}_R}\exp\left(-a_2\left|\lambda_l\right|\right) + \frac{\partial |\lambda_r|}{\partial \dot{x}_R}\exp\left(-a_2\left|\lambda_r\right|\right)\right] \tag{B.10}$$

$$\left.\frac{\partial \boldsymbol{f}_1}{\partial \boldsymbol{x}_2}\right|_{\hat{\boldsymbol{x}}} = \left.\frac{\partial \boldsymbol{f}_1}{\partial \dot{y}_R}\right|_{\hat{\boldsymbol{x}}} = \dot{\psi}_R \tag{B.11}$$

$$\left.\frac{\partial \boldsymbol{f}_1}{\partial \boldsymbol{x}_3}\right|_{\hat{\boldsymbol{x}}} = \left.\frac{\partial \boldsymbol{f}_1}{\partial \dot{\psi}_R}\right|_{\hat{\boldsymbol{x}}} = \dot{y}_R + \frac{2a_1a_2}{m}\left[\frac{\partial |\lambda_l|}{\partial \dot{\psi}_R}\exp\left(-a_2\left|\lambda_l\right|\right) + \frac{\partial |\lambda_r|}{\partial \dot{\psi}_R}\exp\left(-a_2\left|\lambda_r\right|\right)\right] \tag{B.12}$$

$$\left.\frac{\partial \boldsymbol{f}_1}{\partial \boldsymbol{x}_4}\right|_{\hat{\boldsymbol{x}}} = \left.\frac{\partial \boldsymbol{f}_1}{\partial \omega_r}\right|_{\hat{\boldsymbol{x}}} = \frac{2a_1a_2}{m}\frac{\partial\left|\lambda_r\right|}{\partial \omega_r}\exp\left(-a_2\left|\lambda_r\right|\right) \tag{B.13}$$

$$\left.\frac{\partial \boldsymbol{f}_1}{\partial \boldsymbol{x}_5}\right|_{\hat{\boldsymbol{x}}} = \left.\frac{\partial \boldsymbol{f}_1}{\partial \omega_l}\right|_{\hat{\boldsymbol{x}}} = \frac{2a_1a_2}{m6.}\frac{\partial\left|\lambda_l\right|}{\partial \omega_r}\exp\left(-a_2\left|\lambda_l\right|\right) \tag{B.14}$$

$$\left.\frac{\partial \boldsymbol{f}_1}{\partial \boldsymbol{x}_6}\right|_{\hat{\boldsymbol{x}}} = \left.\frac{\partial \boldsymbol{f}_1}{\partial a_1}\right|_{\hat{\boldsymbol{x}}} = \frac{2}{m}\left[sign\left(\lambda_l\right) + sign\left(\lambda_r\right) - \exp\left(-a_2\left|\lambda_l\right|\right) - \exp\left(-a_2\left|\lambda_r\right|\right)\right] \tag{B.15}$$

$$\left.\frac{\partial \boldsymbol{f}_1}{\partial \boldsymbol{x}_7}\right|_{\hat{\boldsymbol{x}}} = \left.\frac{\partial \boldsymbol{f}_1}{\partial a_2}\right|_{\hat{\boldsymbol{x}}} = \frac{2a_1}{m}\left[\left|\lambda_l\right|\exp\left(-a_2\left|\lambda_l\right|\right) + \left|\lambda_r\right|\exp\left(-a_2\left|\lambda_r\right|\right)\right] \tag{B.16}$$

B.2.2 Partial Derivatives for Second State

$$\boldsymbol{f}_2 = -\dot{\psi}_R\dot{x}_R - \frac{b}{m}\left(\beta_1 + \beta_2 - \beta_3 - \beta_4\right) \tag{B.17}$$

$$\left.\frac{\partial \boldsymbol{f}_2}{\partial \boldsymbol{x}_1}\right|_{\hat{\boldsymbol{x}}} = \left.\frac{\partial \boldsymbol{f}_2}{\partial \dot{x}_R}\right|_{\hat{\boldsymbol{x}}} = -\dot{\psi}_R - \frac{b}{m}\left(\frac{\partial\beta_1}{\partial\dot{x}_R} + \frac{\partial\beta_2}{\partial\dot{x}_R} - \frac{\partial\beta_3}{\partial\dot{x}_R} - \frac{\partial\beta_4}{\partial\dot{x}_R}\right) \tag{B.18}$$

$$\left.\frac{\partial \boldsymbol{f}_2}{\partial \boldsymbol{x}_2}\right|_{\hat{\boldsymbol{x}}} = \left.\frac{\partial \boldsymbol{f}_2}{\partial \dot{y}_R}\right|_{\hat{\boldsymbol{x}}} = -\frac{b}{m}\left(\frac{\partial\beta_1}{\partial\dot{y}_R} + \frac{\partial\beta_2}{\partial\dot{y}_R} - \frac{\partial\beta_3}{\partial\dot{y}_R} - \frac{\partial\beta_4}{\partial\dot{y}_R}\right) \tag{B.19}$$

$$\left.\frac{\partial \boldsymbol{f}_2}{\partial \boldsymbol{x}_3}\right|_{\hat{\boldsymbol{x}}} = \left.\frac{\partial \boldsymbol{f}_2}{\partial \dot{\psi}_R}\right|_{\hat{\boldsymbol{x}}} = -\dot{x}_R - \frac{b}{m}\left(\frac{\partial\beta_1}{\partial\dot{\psi}_R} + \frac{\partial\beta_2}{\partial\dot{\psi}_R} - \frac{\partial\beta_3}{\partial\dot{\psi}_R} - \frac{\partial\beta_4}{\partial\dot{\psi}_R}\right) \tag{B.20}$$

$$\left.\frac{\partial \boldsymbol{f}_2}{\partial \boldsymbol{x}_8}\right|_{\hat{\boldsymbol{x}}} = \left.\frac{\partial \boldsymbol{f}_2}{\partial b}\right|_{\hat{\boldsymbol{x}}} = -\frac{b}{m}\left(\beta_1 + \beta_2 - \beta_3 - \beta_4\right) \tag{B.21}$$

B.2.3 Partial Derivatives for Third State

$$\boldsymbol{f}_3 = \frac{2a_1 W}{I}\begin{pmatrix} sign\left(\lambda_l\right) - sign\left(\lambda_r\right) \\ \\ -\exp\left(-a_2\left|\lambda_l\right|\right) + \exp\left(-a_2\left|\lambda_r\right|\right) \end{pmatrix} - \frac{bL}{I}\begin{pmatrix} \beta_1 + \beta_2 \\ \\ -\beta_3 - \beta_4 \end{pmatrix} \tag{B.22}$$

$$\begin{aligned}\left.\frac{\partial \boldsymbol{f}_3}{\partial \boldsymbol{x}_1}\right|_{\hat{\boldsymbol{x}}} = \left.\frac{\partial \boldsymbol{f}_3}{\partial \dot{x}_R}\right|_{\hat{\boldsymbol{x}}} =& \frac{2a_1 a_2 W}{I}\left[\frac{\partial\left|\lambda_l\right|}{\partial \dot{x}_R}\exp\left(-a_2\left|\lambda_l\right|\right) - \frac{\partial\left|\lambda_r\right|}{\partial \dot{x}_R}\exp\left(-a_2\left|\lambda_r\right|\right)\right] \\ & - \frac{bL}{I}\left(\frac{\partial \beta_1}{\partial \dot{x}_R} + \frac{\partial \beta_2}{\partial \dot{x}_R} - \frac{\partial \beta_3}{\partial \dot{x}_R} - \frac{\partial \beta_4}{\partial \dot{x}_R}\right)\end{aligned} \tag{B.23}$$

$$\left.\frac{\partial \boldsymbol{f}_3}{\partial \boldsymbol{x}_2}\right|_{\hat{\boldsymbol{x}}} = \left.\frac{\partial \boldsymbol{f}_3}{\partial \dot{y}_R}\right|_{\hat{\boldsymbol{x}}} = -\frac{bL}{I}\left(\frac{\partial \beta_1}{\partial \dot{y}_R} + \frac{\partial \beta_2}{\partial \dot{y}_R} - \frac{\partial \beta_3}{\partial \dot{y}_R} - \frac{\partial \beta_4}{\partial \dot{y}_R}\right) \tag{B.24}$$

$$\begin{aligned}\left.\frac{\partial \boldsymbol{f}_3}{\partial \boldsymbol{x}_3}\right|_{\hat{\boldsymbol{x}}} = \left.\frac{\partial \boldsymbol{f}_3}{\partial \dot{\psi}_R}\right|_{\hat{\boldsymbol{x}}} =& \frac{2a_1 a_2 W}{I}\left[\frac{\partial\left|\lambda_l\right|}{\partial \dot{\psi}_R}\exp\left(-a_2\left|\lambda_l\right|\right) - \frac{\partial\left|\lambda_r\right|}{\partial \dot{\psi}_R}\exp\left(-a_2\left|\lambda_r\right|\right)\right] \\ & - \frac{bL}{I}\left(\frac{\partial \beta_1}{\partial \dot{\psi}_R} + \frac{\partial \beta_2}{\partial \dot{\psi}_R} - \frac{\partial \beta_3}{\partial \dot{\psi}_R} - \frac{\partial \beta_4}{\partial \dot{\psi}_R}\right)\end{aligned} \tag{B.25}$$

$$\left.\frac{\partial \boldsymbol{f}_3}{\partial \boldsymbol{x}_4}\right|_{\hat{\boldsymbol{x}}} = \left.\frac{\partial \boldsymbol{f}_3}{\partial \omega_r}\right|_{\hat{\boldsymbol{x}}} = -\frac{2a_1 a_2 W}{I}\left[\frac{\partial\left|\lambda_r\right|}{\partial \omega_r}\exp\left(-a_2\left|\lambda_r\right|\right)\right] \tag{B.26}$$

$$\left.\frac{\partial \boldsymbol{f}_3}{\partial \boldsymbol{x}_5}\right|_{\hat{\boldsymbol{x}}} = \left.\frac{\partial \boldsymbol{f}_3}{\partial \omega_l}\right|_{\hat{\boldsymbol{x}}} = \frac{2a_1 a_2 W}{I}\left[\frac{\partial\left|\lambda_l\right|}{\partial \omega_l}\exp\left(-a_2\left|\lambda_l\right|\right)\right] \tag{B.27}$$

$$\left.\frac{\partial \boldsymbol{f}_3}{\partial \boldsymbol{x}_6}\right|_{\hat{\boldsymbol{x}}} = \left.\frac{\partial \boldsymbol{f}_3}{\partial a_1}\right|_{\hat{\boldsymbol{x}}} = \frac{2W}{I}\left[sign\left(\lambda_l\right) - sign\left(\lambda_r\right) - \exp\left(-a_2\left|\lambda_l\right|\right) + \exp\left(-a_2\left|\lambda_r\right|\right)\right] \tag{B.28}$$

$$\left.\frac{\partial \boldsymbol{f}_3}{\partial \boldsymbol{x}_7}\right|_{\hat{\boldsymbol{x}}} = \left.\frac{\partial \boldsymbol{f}_3}{\partial a_2}\right|_{\hat{\boldsymbol{x}}} = \frac{2a_1W}{I}\left[\left|\lambda_l\right|\exp\left(-a_2\left|\lambda_l\right|\right) - \left|\lambda_r\right|\exp\left(-a_2\left|\lambda_r\right|\right)\right] \tag{B.29}$$

$$\left.\frac{\partial \boldsymbol{f}_3}{\partial \boldsymbol{x}_8}\right|_{\hat{\boldsymbol{x}}} = \left.\frac{\partial \boldsymbol{f}_3}{\partial b}\right|_{\hat{\boldsymbol{x}}} = -\frac{L}{I}\left(\beta_1 + \beta_2 - \beta_3 - \beta_4\right) \tag{B.30}$$

B.2.4 Partial Derivatives of the Fourth State

$$\boldsymbol{f}_4 = k_\omega\left(\omega_{c,r} - \omega_r\right) \tag{B.31}$$

$$\left.\frac{\partial \boldsymbol{f}_4}{\partial \boldsymbol{x}_4}\right|_{\hat{\boldsymbol{x}}} = \left.\frac{\partial \boldsymbol{f}_4}{\partial \omega_r}\right|_{\hat{\boldsymbol{x}}} = -k_\omega \tag{B.32}$$

B.2.5 Partial Derivatives of the Fifth State

$$\boldsymbol{f}_5 = k_\omega\left(\omega_{c,l} - \omega_l\right) \tag{B.33}$$

$$\left.\frac{\partial \boldsymbol{f}_5}{\partial \boldsymbol{x}_5}\right|_{\hat{\boldsymbol{x}}} = \left.\frac{\partial \boldsymbol{f}_5}{\partial \omega_l}\right|_{\hat{\boldsymbol{x}}} = -k_\omega \tag{B.34}$$

LIST OF REFERENCES

[1] Lee Ewing. Strong Growth Predicted for Ground Robots Designed for Agriculture. *Mission Critical: Agriculture 2014 by Association for Unmanned Vehicle Systems*, 4(2):13 – 15, 2014.

[2] Fuhong Dong, Wolfgang Heinemann, and Roland Kasper. Development of a row guidance system for an autonomous robot for white asparagus harvesting. *Computers and Electronics in Agriculture*, 79(2):216–225, 2011.

[3] Shigehiko Hayashi, Kenta Shigematsu, Satoshi Yamamoto, Ken Kobayashi, Yasushi Kohno, Junzo Kamata, and Mitsutaka Kurita. Evaluation of a strawberry-harvesting robot in a field test. *Biosystems Engineering*, 105(2):160–171, 2010.

[4] Keyvan Vakilian Asefpour and Jafar Massah. Design, development and performance evaluation of a robot to early detection of nitrogen deficiency in greenhouse cucumber (cucumis sativus) with machine vision. *International Journal of Agriculture: Research and Review.*, 2(4):448–454, 2012.

[5] Sindhuja Sankaran, Ashish Mishra, Reza Ehsani, and Cristina Davis. A review of advanced techniques for detecting plant diseases. *Computers and Electronics in Agriculture*, 72(1):1–13, 2010.

[6] David Pimentel, Rodolfo Zuniga, and Doug Morrison. Update on the environmental and economic costs associated with alien-invasive species in the United States. *Ecological Economics*, 52(3 SPEC. ISS.):273–288, 2005.

[7] Gianni Campion, Georges Bastin, and Brigitte D'Andréa-Novel. Structural properties and classification of kinematic and dynamic models of wheeled mobile robots. *IEEE Transactions on Robotics and Automation*, 12(1):47–62, 1996.

[8] L. Caracciolo, a. de Luca, and S. Iannitti. Trajectory tracking control of a four-wheel differentially driven mobile robot. *Proceedings 1999 IEEE International Conference on Robotics and Automation (Cat. No.99CH36288C)*, 4(May):2632–2638, 1999.

[9] Jingang Yi, Hongpeng Wang, Junjie Zhang, Dezhen Song, Suhada Jayasuriya, and Jingtai Liu. Kinematic modeling and analysis of skid-steered mobile robots with applications to low-cost inertial-measurement-unit-based motion estimation. *IEEE Transactions on Robotics*, 25(5):1087–1097, 2009.

[10] F Wu, Z Guan, and A Whidden. Strawberry industry overview and outlook. *. ifas. ufl. edu/pdf/webinar/Strawberry. . . .*, 2012.

[11] M. G. (Mieczyslaw Gregory) Bekker. *Theory of land locomotion*. University of Michigan Press, 1956.

[12] J. Y. (Jo Yung) Wong. *Theory of ground vehicles*. John Wiley, 2001.

[13] Zhenzhong Jia, William Smith, and Huei Peng. Terramechanics-based wheelterrain interaction model and its applications to off-road wheeled mobile robots. *Robotica*, 30(03):491–503, 2011.

[14] Genya Ishigami, Akiko Miwa, Keiji Nagatani, and Kazuya Yoshida. Terramechanics-based model for steering maneuver of planetary exploration rovers on loose soil. *Journal of Field Robotics*, 24(3):233–250, 2007.

[15] Alfred Gray, Elsa Abbena, and Simon Salamon. Torus Knots. In *Modern Differential Geometry*, chapter 7.7, pages 211–213. Taylor & Francis, 1995.

[16] Jo-Yung Wong and A.R. Reece. Prediction of Rigid Wheel Performance Based on the Analysis of Soil-Wheel Stresses Part I. Performance of Driven Rigid Wheel. *Journal of Terramechanics*, 4(1):81–88, 1967.

[17] T. H. Tran, N. M. Kwok, S. Scheding, and Q. P. Ha. Dynamic modelling of wheel-terrain interaction of a UGV. *Proceedings of the 3rd IEEE International Conference on Automation Science and Engineering, IEEE CASE 2007*, pages 369–374, 2007.

[18] Jingang Yi and Zane Goodwin. Adaptive Trajectory Tracking Control of Skid-Steered Mobile Robots. (April):10–14, 2007.

[19] Chris C Ward and Karl Iagnemma. A Dynamic-Model-Based Wheel Slip Detector for Mobile Robots on Outdoor Terrain. 24(4):821–831, 2008.

[20] O Onafeko and AR Reece. Soil stresses and deformations beneath rigid wheels. *Journal of Terramechanics*, 1967.

[21] Dan Simon. *Optimal State Estimation*, volume 2. 2006.

[22] WH Press. *Numerical recipes 3rd edition: The art of scientific computing*. 2007.